Long-term Variability in Black Carbon Emissions Constrained by Gap-filled Absorption Aerosol Optical Depth and Associated Premature Mortality in China

Wenxin Zhao[1], Yu Zhao[1,2*], Yu Zheng[3], Dong Chen[4], Jinyuan Xin[5], Kaitao Li[6], Huizheng Che[3], Zhengqiang Li[7], Mingrui Ma[1], Yun Hang[8]

1 State Key Laboratory of Pollution Control and Resource Reuse, School of Environment, Nanjing University, 163 Xianlin Rd., Nanjing, Jiangsu 210023, China

2 Jiangsu Collaborative Innovation Center of Atmospheric Environment and Equipment Technology (CICAEET), Nanjing University of Information Science and Technology, Jiangsu 210044, China

3 State Key Laboratory of Severe Weather (LASW) & Key Laboratory of Atmospheric Chemistry of CMA (LAC), Chinese Academy of Meteorological Sciences, Beijing 100081, China

4 Jiangsu Provincial Academy of Environmental Science, 176 North Jiangdong Rd., Nanjing, Jiangsu 210036, China

5 LAPC, Institute of Atmospheric Physics, Chinese Academy of Sciences, Beijing 100029, China

6 School of Information, Space Engineering University, Beijing 101416, China

7 State Environmental Protection Key Laboratory of Satellite Remote Sensing, Aerospace Information Research Institute, Chinese Academy of Sciences, Beijing 100101, China

8 Gangarosa Department of Environment Health, Rollins School of Public Health, Emory University, 1518 Clifton Road NE, Atlanta, GA 30322, USA

* Corresponding Author: Yu Zhao

Phone: 86-25-89680650; email: yuzhao@nju.edu.cn

Abstract

Black carbon (BC) plays an important role in air quality, public health, and climate, while its long-term variations in emissions and health effect were insufficiently understood for China. Here, we present the spatiotemporal evolution of BC emissions and the associated premature mortality in China during 2000-2020, based on an integrated framework combining satellite observations from Ozone Monitoring Instrument (OMI), an Extreme Gradient Boosting (XGBoost) algorithm, a "top-down" inversion approach, and an exposure-response model. We found that the "bottom-up" approach likely underestimated BC emissions, particularly in less developed western and remote areas. Pollution controls were estimated to reduce the annual BC emissions by 26% during 2010-2020, reversing the 8% growth during 2000-2010. BC emissions in the main coal-producing provinces declined by 2010 but rebounded afterwards. By contrast, provinces with higher economic and urbanization levels experienced emission growth (0.05-0.10 $Mg/km^2/yr$) by 2010 and declined greatly (0.07-0.23 $Mg/km^2/yr$) during 2010-2020. The national annual BC-associated premature mortality ranged between 733,910 (95% confidence interval: 676,790-800,250) and 937,980 cases (864,510-1,023,400) for different years. The changing BC emissions contributed 78,590 cases (72,520-85,600) growth within 2000-2005 and 133,360 (123,150-145,180) reduction within 2010-2015. Strategies differentiated by region are needed for further reducing BC emissions and its health and climate impacts.

1. Introduction

Black carbon (BC), commonly emitted during incomplete combustion of fossil fuels (Bond et al., 2013; Liu et al., 2022; Shindell et al., 2012), is an important species in airborne fine particulate matter ($PM_{2.5}$). BC poses greater health risks than total $PM_{2.5}$ due to its absorption of harmful matters (polycyclic aromatic hydrocarbons and volatile organic compounds), and penetration abilities (Li et al., 2016b; Pani et al., 2020; Wang et al., 2014; Xue et al., 2021), and is a crucial short-lived climate forcer (Harmsen et al., 2020; Samset et al., 2020). With a large population and high energy consumption, China has become a major contributor of global BC emissions (Lu et al., 2019; Wang et al., 2012) and has suffered from BC-associated climate and health effects since the 2000s (Gu et al., 2020; Liu et al., 2022). Compared to widely measured total $PM_{2.5}$ across the country (Liang et al., 2020; Zhang et al., 2019), fewer BC data are available from ground observations and the spatiotemporal coverage of BC concentrations is far less sufficient (Cui et al., 2015; Tao et al., 2017). As a result, the long-term evolution of BC pollution and its associated health burden remain unclear.

Alternatively, satellite observations provide broader spatiotemporal coverage of aerosol-related variables (Schutgens et al., 2021), e.g., aerosol absorption optical depth (AAOD) that reflects light extinction due to light-absorption aerosols including BC. However, most sensors can only monitor total aerosol information rather than individual components (Li et al., 2016a), and cloud cover and surface reflectance cause considerable missing values and uncertainty (Liang et al., 2020; Zhang et al., 2015). For example, Ozone Monitoring

Instrument (OMI; Deborah and Pepijn, 2012; https://disc.gsfc.nasa.gov/datasets/OMAEROe_003/summary; last accessed on 10 March 2022) and POLarization and Directionality of the Earth's Reflectance instrument (POLDER; https://www.grasp-open.com; last accessed on 4 May 2022) provided long-term national average AAOD coverage of 9%-22% (2005-2020) and 8%-12% (2006-2013) in China, respectively. Satellite-derived AAOD needs to be comprehensively processed to fill gaps in its data and to improve its representativeness of BC before it can be effectively applied.

Complete and reliable emission estimates are essential for diagnosing pollution sources and evaluating the benefits of pollution controls. Compared to species generated largely from industrial and energy infrastructures (e.g., SO_2 and NO_X), BC emissions are more challenging to estimate as they are commonly from residential and commercial sources that are more difficult to track (Bond et al., 2013; Li et al., 2017; Zhu et al., 2019). Existing "bottom-up" estimates, varied between 0.9 and 2.5 Tg/yr during 2000-2020, with inconsistent interannual changing patterns (the Multiresolution Emission Inventory for China (MEIC; Tsinghua University, 2023); the Emissions Database for Global Atmospheric Research (EDGAR; European Commission, 2022); Community Emissions Data System (CEDS; Mcduffie et al., 2020); the Peking University Fuel Inventory (PKU-Fuel; Wang et al., 2014); Regional Emission inventory in ASia (REAS; Kurokawa and Ohara, 2020); and others (Lu et al., 2011; Lei et al., 2011; Klimont et al., 2009; Qin and Xie, 2012)). The uncertainty of those estimates reached up to ±360% due to diverse and quickly changing manufacturing technologies and emission controls (Streets et al., 2003; Wang et al., 2016). Consequently, chemical transport models (CTMs) often underestimate BC concentrations and AAOD, particularly in Asia, ranging from factors of 2-10 (Chen et al., 2019c; Hu et al., 2016; Wang, 2015). To overcome this limitation, "top-down" approaches constraining BC emissions with available observations have been developed and applied to correct BC emissions in China (Cohen and Wang, 2014; Evangeliou et al., 2018; Fu et al., 2012; Guerrette and Henze, 2017; Wang et al., 2013; Zhao et al., 2019). However, restricted by insufficient spatiotemporal coverage, studies were usually conducted for individual years/months and showed considerable discrepancies (Wang et al., 2018; Zhang et al., 2015). Incomplete and inconsistent information could hardly be combined to provide full knowledge of long-term BC emissions. Based on the "bottom-up" emission estimates with great uncertainty and CTMs, previous studies have evaluated the BC-associated premature mortality in China for limited years (2000, 2013, and 2016, Cui et al., 2022; Qin et al., 2019; Saikawa et al., 2009; Wang et al., 2021). Moreover, the results showed magnitude discrepancy (50,100-1,436,960 cases) and few analyses have evaluated the long-term spatiotemporal variations and driving forces of BC-associated health effects. The influence of human activities on quickly changing BC emissions and their associated health impact is inadequately or inaccurately understood, weakening science-based decision making for air pollution control.

Herein, we developed an integrated framework combining available satellite observations, an improved machine learning technique, a "top-down" inversion approach, and an exposure-response model to obtain a panoramic perspective of China's BC emissions and the associated mortality for the past two decades. We first predicted full-coverage monthly AAOD for mainland China during 2000-2020 using an Extreme Gradient Boosting (XGBoost) model. Combining this new dataset with air quality and BC light absorption empirical models, we then improved the "top-down" inversion technique to estimate the interannual changes in BC emissions. We further calculated the BC-associated premature mortality and attributed its interannual changes to individual driving factors. The outcomes highlight an improved BC emission estimation and the influence of human activities on the long-term evolution of BC emissions and the associated health effects, thereby supporting policies coordinating air quality, health, and climate issues.

2. Materials and Methods

2.1 Filling gaps in AAOD data using a machine learning algorithm

We applied the XGBoost model to fill gaps in satellite-derived AAOD data at the monthly level during 2000-2020. XGBoost has been widely used in predicting air pollution and shown to outperform various statistical and machine learning models (Liang et al., 2020; Liu et al., 2022; Wang et al., 2023; Xiao et al., 2018). The XGBoost algorithm is an additive model based on hundreds of decision tree models. It first builds multiple Classification and Regression Trees, and then integrates these trees as a new tree model using an additive function (Liu et al., 2021). The model continues to iteratively improve, and the new tree model generated in each iteration will fit the residual of the previous tree. The complexity of the ensemble model will gradually increase until the training achieves the best results.

Different from the boosting approach of XGBoost, the Random Forest model fits a set of decision trees, and then a majority vote method is taken for final prediction (Lyu et al., 2019). Generally, XGBoost model requires less training and prediction time and presents better performance than the Random Forest model. The target domain included mainland China at a horizontal resolution of 0.25° × 0.25° (Supplementary Figure S1).

OMI takes advantage of the near-UV algorithm based on the sensitivity of radiances measured at the atmosphere to the varying aerosol species to derive AAOD (Zhang et al., 2017). The algorithm excluded the very small AOD values to reduce the uncertainty of the AAOD retrieval at low AOD values. Previous studies have proven the good agreement between OMI AAOD and AERONET ground observations as well as other satellite observations (Ahn et al., 2008; Zhang et al., 2017). Here we used OMI-derived AAOD at 483 nm, obtained from the OMAEROe L3 global aerosol product at a horizontal resolution of 0.25° × 0.25° (Deborah and Pepijn, 2012; https://disc.gsfc.nasa.gov; last accessed on 10 March 2022), as the dependent variable for model training and validation. For each grid cell, daily AAOD values for no less than 7 days in a given month were averaged as the monthly AAOD value. Owing to its long service time and damage to the satellite sensor, the original spatial coverage of monthly OMI-derived AAOD ranged from 1% to 53%, and was commonly lower for later years than earlier years. The multiyear average coverage was relatively low in southern China (<25%), attributed to cloud cover and high surface reflectance (Supplementary Figure S2).

Twenty-four interpretation variables were selected for model training, including aerosol optical, meteorological, geographic, and temporal parameters (Supplementary Table S1). Aerosol optical and meteorological parameters were extracted from the Modern-Era Retrospective analysis for Research and Applications, Version 2 (MERRA-2) dataset at a horizontal resolution of 0.625° × 0.5° (https://disc.gsfc.nasa.gov; last accessed on 10 June 2022), to reflect the optical properties, transport, and diffusion of pollutants. Here we use the daily MERRA-2 data because the daily average MERRA-2 data was proved more reliable than the hourly data compared to the observation (Xu et al., 2020). As ancillary variables associated with BC emission sources and transport conditions, land-use data were obtained from the Institute of Geographic Sciences and Natural Resources Research, Chinese Academy of Sciences at a horizontal resolution of 1 × 1 km (https://www.resdc.cn/DOI/DOI.aspx?DOIID=129; last accessed on 25 June 2022). The elevation data were obtained from the Shuttle Radar Topography Mission at a horizontal resolution of 1 × 1 km (https://www.resdc.cn/data.aspx?DATAID=123; last accessed on 25 June 2022). These parameters were resampled to the 0.25° × 0.25° grid system by averaging the 1-km resolution data. Details for specific feature selection can be found in Supplementary Text S1.

For model performance evaluation, we applied a ten-fold Cross-Validation (CV) firstly to evaluate out-of-sample accuracy. The CV process randomly split training data records into 10 subsets, in which 9 subsets were used to train models and the remaining one was used to examine the performance. Through ten times repetition of CV, all of the data records were tested once. Besides, we collected monthly AAOD data from four aerosol monitoring networks to further verify the model reliability, including Aerosol Robotic Network (AERONET, https://aeronet.gsfc.nasa.gov; last access: 10 March 2022), China Aerosol Remote Sensing Network (CARSNET, Che et al., 2015), Campaign on Atmospheric Aerosol Research Network of China (CARE-China, Xin et al., 2015) and Sun Sky Radiometer Observation Network (SONET, Li et al., 2018), as shown in Supplementary Figure S1a. Detailed site descriptions can be found in corresponding studies. Given the complicated technologies and large costs required for measurement operation, instrument maintenance and calibration, current aerosol monitoring sites are rare and unevenly located in the country. There are clear missing values in time series, and most measurements we collected focused on 2015-2019. All the ground-level AAOD data were interpolated to 483 nm using the Angstrom exponent to independently evaluate the performance of machine learning predictions. Model performance was evaluated with selected statistical indicators including correlation coefficient (R), normalized mean error (NME, Eq. 1), normalized mean bias (NMB, Eq. 2), and root mean squared prediction error (RMSE, Eq. 3).

$$NME = \frac{\sum_{i=1}^{N}|X_i - O_i|}{\sum_{i=1}^{N} O_i} \quad (1)$$

$$NMB = \frac{\sum_{i=1}^{N}(X_i - O_i)}{\sum_{i=1}^{N} O_i} \times 100\% \quad (2)$$

$$RMSE = \sqrt{\frac{1}{N}\sum_{i=1}^{N}(X_i - O_i)^2} \quad (3)$$

Where *X* and *O* indicate the results from XGBoost prediction and OMI observation, respectively. *N* is the number of data points.

2.2 Constraining BC emissions with gap-filled AAOD and CTM

We developed a "top-down" inversion approach to estimate the monthly BC emissions in China during 2000-2020 (see conceptual diagram in Figure 1). To avoid abundant calculations, five-year intervals were adopted in the simulation, and January, April, July, and October were selected as representative months of different seasons (widely applied in previous inversion researches; Zhang et al., 2015; Zhao et al., 2019).

2.2.1 Integrated model for AAOD simulation

We simulated AAOD using the Community Multi-scale Air Quality (CMAQ, USEPA, 2017) model version 5.1 and an empirical BC light absorption model. AAOD is defined as the integrated absorption coefficient (m^{-1}) over the atmospheric column, and the absorption coefficient is the product of the mass concentration (g/m^3) and mass absorption efficiency of BC (MAE, m^2/g) (Bond et al., 2013). Prior anthropogenic BC emissions during 2000-2020 were obtained from MEIC (http://www.meicmodel.org; last accessed on 25 May 2022), and prior BC emissions from open biomass burning (OBB) were obtained from the Global Fire Emissions Database version 4.1s (GFED V4.1s, https://www.geo.vu.nl/~gwerf/GFED/GFED4/; last accessed on 25 May 2022). First, BC concentrations at different vertical layers were simulated using the CMAQ model at a horizontal resolution of 27 × 27 km (see Supplementary Text S2 for model settings). Based on our previous measurements, we then adopted an empirical model to quantify the enhanced light absorption of the coating on BC particles (Chen et al., 2019b), and obtained the simulated BC AAOD:

$$MAE_{i,m,n} = 6.83 - 0.0007 \times (\frac{[NA-PM]_{i,m,n}}{[BC]_{i,m,n}})^2 + 0.08\frac{[NA-PM]_{i,m,n}}{[BC]_{i,m,n}} \quad (4)$$

$$AAOD\_BC\_sim_{i,m,n} = \int_{z0}^{z} MAE_{i,m,n} \times [BC]_{i,j,m.n} \times dz \quad (5)$$

where *MAE*, *AAOD_BC_sim*, and *[BC]* represent the simulated BC MAE, BC AAOD, and BC concentration, respectively; *z* and *z0* represent the simulated top and bottom of the atmosphere (0), respectively; *[NA-PM]* represents the simulated concentration of total non-absorbing matter (i.e., SO_4^{2-}, NO_3^-, and organic carbon, OC); *i* and *j* represent the numbers of grids and vertical layers, respectively; *dz* represents the height of the vertical layer; and *m* and *n* represent the year and month, respectively. All parameters and variables shown in the equations are summarized in Supplementary Table S2.

2.2.2 Inversion system for BC emissions

We developed an inversion system based on the spatiotemporal-dependent relationship between BC emissions and BC AAOD.

As AAOD is attributed to all light-absorbing aerosols, including BC, dust, and brown carbon (BrC), we first separated the contribution of BC to the XGBoost-predicted AAOD obtained in Section 2.1, using the fraction of BC in AAOD obtained from MERRA-2:

$$AAOD\_BC\_xgb_{i,m,n} = AAOD\_xgb_{i,m,n} \times \frac{AAOD\_BC\_merra2_{i,m,n}}{AAOD\_merra2_{i,m,n}} \quad (6)$$

where *AAOD_BC_xgb* represents the separated XGBoost BC AAOD; *AAOD_xgb* represents XGBoost AAOD; *AAOD_BC_merra2* represents MERRA-2 BC AAOD; and *AAOD_merra2* represents MERRA-2 AAOD. The hourly MERRA-2 data at 0.625° × 0.5° were reallocated to the horizontal resolution of CMAQ model (27 km) and averaged to a monthly level.

With XGBoost BC AAOD, we inferred monthly BC emissions with Eq. 7:

$$E_{posterior\ i,m,n} = E_{prior\ i,m,n} \times (1 + \frac{AAOD\_BC\_xgb_{i,m,n} - AAOD\_BC\_sim_{i,m,n}}{AAOD\_BC\_xgb_{i,m,n}} \times \alpha_{i,m,n}) \quad (7)$$

where $E_{posterior}$ and E_{prior} represent posterior and prior BC emissions, respectively; *AAOD_BC_sim* represents the simulated BC AAOD based on prior BC emissions; and α is a unitless factor representing the sensitivity of changes in BC AAOD to those in BC emissions in each model grid. We carried out a perturbation simulation to obtain α:

$$\alpha_{i,m,n} = \frac{\Delta E_{perturbed\ i,m,n}}{E_{prior\ i,m,n}} \div \frac{AAOD\_BC\_sim_{perturbed\ i,m,n} - AAOD\_BC\_sim_{prior\ i,m,n}}{AAOD\_BC\_sim_{prior\ i,m,n}} \quad (8)$$

where *prior* and *perturbed* represent prior and perturbation simulations, respectively; $\Delta E_{perturbed}/E_{prior}$ represents a 10% reduction in prior BC emissions; and $AAOD\_BC\_sim_{perturbed}$ and $AAOD\_BC\_sim_{prior}$ represent the simulated BC AAOD with the perturbation and prior simulation, respectively.

We adopted the posterior BC emissions as the new BC emission input, repeating the simulation until the NME of BC AAOD from CTM and XGBoost was reduced <30%. We evaluated the CMAQ model performance based on our gap-filled AAOD dataset and available observations of surface BC concentrations collected from 64 published researches (Supplementary Table S3). The collected BC concentration observations cover various sampling regions in China and study period from 2000 to 2020. Most studies analyzed BC using well-acknowledged reliable and widely used analyzers, for example, a DRI carbon analyzer or Sunset carbon analyzer. Besides this base case as mentioned above, we conducted four sensitivity tests to recalculate posterior BC emissions, to explore the uncertainty in the inversion (Supplementary Text S3 and Table S4). They respectively applied the estimated AAOD at a longer wavelength of 865 nm (Test 1), the different dust AAOD fractions (Test 2), the adjusted MAE based on observations (Supplementary Table S5; Test 3) and the adjusted simulated BC lifetime (Test 4).

2.3 Estimating the associated mortality burden and determining its drivers

A log-linear model was applied to estimate the attributable fraction (*AF*) of premature mortality to BC exposure (Wang et al., 2021):

$$AF\left(C_{i,m}\right) = 1 - e^{-\beta_{BC}\times\Delta C_{i,m}} \quad (9)$$

where $C_{i,m}$ represents the posterior simulated average BC concentration of four months in year *m* of grid *i*, and $\Delta C_{i,m}$ represents the difference between $C_{i,m}$ and the health impact threshold. Due to the lack of reported BC concentration thresholds in current epidemiological studies (Cui et al., 2022), we applied the 1.25th percentile of BC concentrations (suggested by Pani et al., 2020; Wang et al., 2021) as the threshold (0.02 μg/m^3). β_{BC} represents the concentration–response coefficient. Here, we used a β_{BC} value of 0.0204 (95% confidence interval (CI): 0.0187-0.0224) based on a unique cohort study conducted in eastern China (Chen et al., 2021).

The all-cause premature mortality (M) attributable to BC exposure was calculated using Eq. 10 (Wang et al., 2021):

$$M_{i,s,m} = P_{i,m} \times PS_{s,m} \times B_{s,m} \times AF(C_{i,m}) \quad (10)$$

where *s* represents the population subgroup, *P* represents the population, *PS* represents the proportion of the population subgroup to the national population, and *B* represents the national baseline mortality rate of all-cause diseases. The gridded population data were aggregated from the 1 km population density dataset in WorldPop (WorldPop, 2018;

https://hub.worldpop.org/doi/10.5258/SOTON/WP00675; last accessed on 20 October 2022). We corrected the annual total population using Chinese census data obtained from the State Statistics Bureau (https://data.stats.gov.cn/; last accessed on 20 October 2022). The national average population age structure and baseline mortality rate of all-cause diseases were collected from the Global Burden of Disease study (Cohen et al., 2017; https://vizhub.healthdata.org/gbd-results/; last accessed on 20 October 2022).

We evaluated the impact of each of the four factors in Eq. 10 (three vulnerability factors and BC exposure) on the changing mortality through a series of sensitivity analyses (Cohen et al., 2017; Geng et al., 2021). We established 24 decomposition sequences with the four factors and calculated the mean changing mortality of each factor through all sequences. Moreover, mortality changes attributed to BC exposure were further disaggregated into contributions from BC emissions and meteorological factors using a direct proportion approach with the CMAQ model (Supplementary Text S4).

3. Results and Discussion

3.1 Gap-filled AAOD during 2000–2020

3.1.1 Evaluation of XGBoost model performance

By filling the missing values with XGBoost model, we obtain full coverage of monthly AAOD for China from 2000 to 2020. Evaluated by 10-fold CV, the predicted AAOD shows good agreements with OMI observations, with R of 0.92, RMSE of 0.013 and NMB of -4%

(Figure 2). Comparison with individual ground measurements further verifies the reliability and robustness of the model across regions and periods, with RMSE of 0.017 and NMB of 5% for all available observations (Supplementary Table S8). The comparisons with observations at typical individual sites are shown in Supplementary Figure S5. Overall, better performance is shown by our predictions compared to other AAOD datasets. As a reference, the RMSE and NMB between MERRA-2 and the same observations are 0.021 and -19% (Supplementary Table S8), respectively. In addition to evaluation for the whole period, Supplementary Table S9 shows model performance for each year. The performance of 10-fold CV gets moderately poorer for more recent years, accompanied with the reduced sampling size of OMI observations. Regarding the ground observation, better performance appeared in recent years indicated by the smaller RMSE, and the underestimation in earlier years could probably be attributed to less sites available and more difficulty in data quality control.

Besides, the spatial coverage of OMI AAOD influences the training data size for XGBoost model and thereby the spatiotemporal pattern of gap-filled AAOD. Supplementary Table S10 shows the XGBoost performance against OMI and ground measurement by OMI coverage. In general, poorer performance was found for areas with more missing values. Evaluated against ground measurement, for example, the RMSE and NMB for areas with OMI coverage less than 20% are 0.019 and 9%, and they decline to 0.015 and 3% for areas with OMI coverage more than 60%. All the biases are kept within limited range. The analysis indicates the satisfying quality of our gap-filled AAOD dataset, with full spatiotemporal coverage for the research domain and period.

Supplementary Table S1 summarizes the importance levels of model predictors in the XGBoost model, expressed with three indicators, and “Gain” is the most decisive one. MERRA-2 AAOD, longitude, latitude and temporal parameters are identified as most dominant variables for filling gap of OMI AAOD. Besides, crop coverage is another dominant variable, which reflects the contribution of OBB to light-absorbing aerosol emissions and thereby to AAOD. Specific meteorological parameters, e.g., surface pressure (PS), short-wave radiation flux (SWGDN), evaporation from turbulence (EVAP), and planetary boundary layer height (PBLH), reflect surface energy budget, transport and diffusion of air pollutants, thus play an important role in AAOD prediction.

3.1.2 Spatiotemporal patterns of XGBoost-predicted AAOD during 2000–2020

Figure 3a illustrates the spatial distribution of the averaged XGBoost-predicted AAOD during 2000-2020. Hot spots mainly existed in eastern China, with a regional average of 0.05, which was higher than the national average of 0.03. The AAOD values of Beijing-Tianjin-Hebei (BTH), Fenwei Plain (FWP), Yangtze River Delta (YRD), Sichuan Basin (SCB), and Northeast China (NE) were 1.4-1.8 times that of the national average, while that of Pearl River Delta (PRD) was much closer to the national average (see Figure S1a for the locations of regions). The relatively small proportion of the rural population to the total population (34%) and highly developed economy in PRD might have resulted in limited light-absorbing aerosol emissions.

Figures 3b-h illustrates the interannual variability of the predicted monthly AAOD for China and the key regions during 2000-2020, which were divided into two temporal phases. In phase 1 (2000-2012), the AAOD of China experienced a slight decline (-6.94×10^{-5}/yr) while those of key regions moderately increased, except FWP. The annual AAOD growth of the most economically developed regions (BTH, YRD, and PRD) ranged 1.13×10^{-4}-5.20×10^{-4} /yr, larger than those in other regions (SCB and NE, 2.84×10^{-7}-7.54×10^{-5} /yr), reflecting the influence of regional differences based on human activities and meteorological conditions. Increasing industrial production and residential combustion elevated anthropogenic emissions of light-absorbing aerosols, thereby increasing AAOD values in key regions. However, nationwide increasing precipitation during phase 1 (0.3 $g/m^2/s/yr$ indicated by MERRA-2) may have enhanced the removal of pollutants and offset the effects of increasing emissions. In addition, strengthened afforestation policies in northern China led to a decline in dust aerosol emissions and thus the AAOD values during this period (Middleton, 2019).

In phase 2 (2013-2020), the AAOD of China demonstrated a clear decline (1.99×10^{-4}/yr), with faster rates in key regions (3.61×10^{-4}-1.42×10^{-3}/yr). The AAOD decline in key regions in phase 2 was much faster than its growth in phase 1, indicating the benefits of China's air pollution controls, such as implementation of the strictest ever emission standards in the industrial sector and promotion of clean energy use for household heating and cooking. AAOD growth clearly occurred in northern regions from 2018 onwards, which differed from its continuous decrease in southern regions. The increasing surface wind speed in northern regions elevated the frequency of sandstorms, resulting in greater regional emissions of light-absorbing dust aerosols that partly contributed to AAOD growth (Yang et al., 2021).

3.2 Long-term evolution of constrained BC emissions during 2000–2020

3.2.1 Verification of constrained BC emissions

We find that application of posterior BC emissions constrained by XGBoost-predicted AAOD (described in detail in Section 3.2.2) largely improved the model performance of BC concentration and AAOD simulation compared with use of prior BC emissions.

With acceptable performance of meteorological simulation (Supplementary Table S11), the CMAQ model presented a clear underestimation of surface BC concentrations based on the prior BC emissions, with the NMB and NME calculated to be −46% and 53%, respectively (Figure 4). Besides, larger underestimation appeared for the very early and most recent year, with NMB calculated at -59% and -60% for 2000 and 2020, respectively (Supplementary Figure S6), which may be caused by larger underestimation of BC emissions in these years (described in detail in Section 3.2.2). Application of posterior BC emissions greatly reduced the NMB and NME within the research period to −14% and 36%, respectively (Figure 4). As a reference, the performance meets the benchmark of BC simulation (NMB < ±20% and NME <45%) proposed by Huang et al. (2021). Moreover, improved model performance has been achieved for all the years with largely reduced NMB and NME compared to simulations with the prior emissions (Supplementary Figure S6). Larger uncertainty for 2000 may be caused by limited observation and less-controlled data quality for earlier years.

We also compare the simulated and observed BC concentrations by land use type (Supplementary Figure S7). Application of the prior emissions resulted in more underestimation of BC concentration for the forest and grassland regions (NMB: -51%~-77%; NME: 51%~77%) compared to urban and rural regions (NMB: -35%~-51%; NME: 47%~51%). The model performance was clearly improved for all the land use types when the posterior emissions were applied. In particular the NMB and NME were calculated to respectively range -2%~-40% and 31%~52%, for the forest and grassland regions. The evaluation supported our estimates of posterior emissions, not only for areas with insensitive human activities (e.g., urban regions) but also remote regions.

Similarly, simulation of AAOD based on the prior emissions presented a clear underestimation compared with the OMI-derived observations, with the monthly NMB and NME ranging -85%~-29% and 34%~85%, respectively (Supplementary Table S12). As pointed by Bond et al. (2013), the incorrect assumption of mixing state of BC in the CTM could result in the general underestimation of MAE, and thereby AAOD. Clear improvement in the performance of AAOD simulation can be found when the posterior emissions were applied. The NMB, NME, and RMSE were calculated to range -11%~14%, 15%~28%, and 0.01~0.03, respectively, much smaller than those with the prior emissions, while R was largely elevated from 0.15~0.86 to 0.73~0.95.

3.2.2 Spatiotemporal patterns of posterior BC emissions and differences between prior and posterior BC emissions

Figures 5a–c presents the spatial distribution of multiyear averages of the prior and posterior BC emissions and their relative differences (see details for individual years in Figure 6). The annual total posterior BC emissions were estimated to increase from 6.48 Tg in 2000 to 7.03 Tg in 2010 and decrease to 5.21 Tg in 2020. Compared with the prior BC emissions, the posterior BC emissions presented a clear enhancement, with a multiyear average factor (the ratio of the posterior emission difference to prior BC emissions, i.e., (a posterior – a prior) / a prior) of 3.3 for the entire country (Figure 5c). The value declined from 3.7 to 2.7 during 2000–2015, but rose again to 4.1 in 2020 (Figure 5d). The posterior BC emissions also presented an enhancement compared to other "bottom–up" estimates of China's BC emissions (sum of anthropogenic and OBB emissions), with the lowest factor of 1.7 for the PKU-Fuel (http://inventory.pku.edu.cn/; last accessed on 1 May 2023) and highest factor of 4.1 for EDGAR+GFED (https://edgar.jrc.ec.europa.eu/dataset_ap61; last accessed on 1 May 2023) (Figure 5d and Table 1). The comparisons between "bottom–up" and "top–down" estimates of BC emissions suggested a possible underestimation of the former, resulting partly from the under-reporting of activity levels and lack of local measurements for specific BC emission factors (EFs, emissions per unit of activity level) (Fu et al., 2012; Guan et al., 2012). In addition, the omission of small fires from satellite observations and application of global EFs led to an underestimation of biomass burning emissions (Yang and Zhao, 2019). Along with improved energy and economic statistics and the increased amount of EF data obtained through field observations, the discrepancy between prior and posterior

BC emissions was gradually reduced until 2020. The increased uncertainty in prior BC emissions in 2020 may have resulted partly from an underestimation of increased fuel use owing to residential heating and cooking during the COVID-19 lockdown and quarantine (Zheng et al., 2020).

The posterior emissions presented a smaller interannual variability compared to the prior and other "bottom-up" estimates, with a net growth of 8% during 2000-2010 (the analogous numbers are 12%-55% for various "bottom-up" estimates including 24% for the prior used in this work, MEIC+GFED) and a decline of 26% during 2010-2020 (41% for MEIC+GFED, Figure 5e). Besides residential sources, prior emission estimate bias may also have occurred in the transportation sector, such as extra emissions derived from inadequately eliminated vehicles with relatively old standards and the use of specific after-treatment technologies (e.g., diesel particulate filters) causing the release of ultrafine particles (Louis et al., 2016).

Relatively smaller differences between posterior and prior BC emissions were found in eastern China, with a multiyear average of posterior to prior BC emission ratio estimated at 2.4, while that for the rest of China reached 8.0 (Figure 5f). The relative differences between posterior and other "bottom-up" BC emission estimates were smaller (1.1-2.1) in more economically developed regions (BTH, FWP, YRD, and PRD), but larger (3.5-5.6) in SCB, NE, and other regions (Table 1). To further explore the impact of human activities on BC emissions, we divided the country into different land use types (Supplementary Figure S1b). The multiyear average BC emission intensity in urban areas was estimated at 1.86 $Mg/km^2/yr$, higher than 1.47 $Mg/km^2/yr$ in rural areas (Table 2). Industrial production, transportation, and commercial activities generate abundant emissions in urban areas, while straw burning, residential cooking, and heating are important emission sources in rural areas. Smaller BC emission intensity was estimated in regions less influenced by human activities, i.e., 0.84, 0.33, and 0.11 Mg/km^2/yr for forest, grassland, and unused regions, respectively. As shown in Figure 5f, the relative differences between posterior and prior BC emissions were smallest in urban areas, with a multiyear average enhancement factor of 1.6, followed by rural areas (factor of 2.6), forest (factor of 4.3), and grassland (factor of 5.5). In general, the "bottom-up" approach could capture information about energy consumption and pollution controls more easily and accurately in regions with more intensive human activities. Such advantages helped reduce the uncertainty in emission estimates for developed urban areas compared with that in remote areas. However, current official statistics do not sufficiently report biofuel consumption and are believed to greatly underestimate raw coal consumption in rural areas (Zhi et al., 2017; Zhu et al., 2019). Limited small fire detection ability via satellite also led to an underestimation of OBB in forest and grassland areas (Schroeder et al., 2008; Yang and Zhao, 2019). Such limitations resulted in a greater underestimation of prior BC emissions in rural and remote regions compared to urban regions (Figure S7).

Previous limited studies employing "top-down" approaches estimated China's BC emissions at 5.7, 3.1, and 2.5 Tg/yr for 2000, 2006, and 2008 (Cohen and Wang, 2014; Fu et al., 2012; Wang et al., 2016), respectively. These studies presented an 0.6-5 times enhancement of posterior BC emissions compared to prior BC emissions (Chen et al., 2019a; Cohen and Wang, 2014; Fu et al., 2012; Wang et al., 2016; Zhang et al., 2015), showing a wider range than the results presented in the current study (2.7-4.1). This discrepancy may have resulted from the application of different inversion approaches, observational data, and prior BC emissions. Moreover, the posterior BC emissions applied in previous studies were lower than those used in the current study for corresponding years by a factor of 12%–64%. In general, incomplete spatial coverage in previous studies limited the emission inversion capability in regions far away from observational sites.

3.2.3 Influence of social and economic development on BC emissions

To explore the influence of social and economic development on BC emissions, we analyzed the diverse changing patterns in posterior BC emission intensity (Mg/km^2) by province, based on rural population fraction, provincial proportion of coal production to the national total, and industrial gross domestic product (GDP).

Shanxi, Inner Mongolia, Henan, and Shaanxi were identified as the main coal-producing provinces, collectively contributing 50% and 68% to national total coal production in China during 2000-2010 and 2010-2020, respectively. Shanxi, Henan, and Shaanxi experienced a decline in posterior BC emission intensity during 2000-2010, with annual average decreasing rates estimated at 0.13, 0.03, and 0.02 Mg/km^2/yr, respectively (Figure 7a). These provinces have long suffered air pollution from coal burning and the coal industry's structure and technology were improved earlier than in other provinces. For example, Shanxi eliminated over 7000 small coal mines and an outdated production capacity of 385 million tons of coal during 2000-2010 (The Central People's Government of the People's Republic of China, 2011;

Han and Wang, 2015). These measures significantly improved coal consumption efficiency, resulting in a sharp decline in BC emission intensity.

In comparison, slower decline or even growth in BC emission intensity was demonstrated in Shanxi and Henan during 2010-2020, with changing rates of −0.007 and 0.004 $Mg/km^2/yr$, respectively (Figure 7b). Merging and reorganization of the coal industry in these two provinces enhanced coal production and consumption in recent years, thereby reducing the benefits of BC emission controls. Comparatively faster declines were demonstrated in Inner Mongolia and Shaanxi, with decreasing rates of 0.01 and 0.03 $Mg/km^2/yr$, respectively (Figure 7b). The proportion of coal production in Inner Mongolia and Shaanxi increased from 8% and 2% in 2000 to 28% and 17% in 2020, respectively, demonstrating the increasingly important role of national coal production in these two provinces (Figures 7c and d). Compared with Shanxi and Henan, relatively later but greater efforts were made to improve the coal industry's structure in Inner Mongolia and Shaanxi, leading to considerable BC emission reductions after 2010.

Increasing emission intensities were found for most other provinces during 2000-2010, particularly those with high industrial GDP (larger circles in Figure 7c). Prominent BC emission intensity growth was demonstrated in Jiangsu, Shandong, and Beijing, with the annual average growth rates ranging from 0.05 to 0.10 $Mg/km^2/yr$. Intensive industrial production activities in these provinces/cities resulted in quickly increasing emissions. Second to industry-developed regions, Anhui, Guangxi, and Yunnan experienced BC emission growth rates of 0.03-0.05 $Mg/km^2/yr$. In these provinces with higher rural population fractions, the enhanced consumption of household solid fuel and limited progress in air pollution controls led to fast BC emission growth, along with increased demand for living standard improvements.

During 2010-2020, BC emission intensities were estimated to decline for most provinces (Figure 7b), and faster decline commonly occurred in provinces with higher urbanization and industrial GDP levels (darker blue and larger circles from right to left on the x-axis in Figure 7d). The greatest reductions were demonstrated in Shanghai, Liaoning, Chongqing, Jiangsu, and Fujian, with the decreasing rate ranging from 0.07 to 0.23 $Mg/km^2/yr$. Within this period, stringent pollution controls in the industrial and transportation sectors took effect, particularly in economically developed and highly urbanized regions, resulting in a faster decline in BC emissions compared with less developed regions. Meanwhile, reduced rural population proportion and increased clean energy use jointly restrained household BC emissions.

3.2.4 Comparison of emission and concentration trends for multiple species

We compare the interannual changes in posterior BC emissions with those in national $PM_{2.5}$, OC, and BC emissions (i.e., prior BC emissions) derived from MEIC, $PM_{2.5}$ concentrations derived from Tracking Air Pollution in China (http://tapdata.org.cn/; last accessed on 31 January 2023), and CMAQ-simulated BC concentrations based on posterior BC emissions (Figure 8). During 2005-2020, the annual BC emissions were estimated to decline by 26% (posterior BC emissions) or 43% (prior BC emissions), which was slower than $PM_{2.5}$ (56%), and the relative reduction in BC concentration (14%) was less than that in $PM_{2.5}$ (35%). Compared to total $PM_{2.5}$, for which the health effects are widely recognized, more attention should be paid to the health effects and control of BC emissions, given its relatively slower decline in ambient concentrations and well-acknowledged higher health risks (Wang et al., 2021; see our estimate on the mortality attributable to BC exposure in Section 3.3). Moreover, the comparison between emission trends in warming (BC) and cooling (e.g., OC) species reveals a climate challenge. Faster decline in OC emissions (47% during 2005-2020) was estimated than in BC emissions, resulting mainly from greatly reduced biofuel use and biomass burning. In contrast, development of the transportation and industrial sectors makes further reductions in BC emissions challenging, and more effective strategy on BC emission controls are urgently needed to restrain climate warming in the future.

3.3 Mortality attributable to BC exposure and its drivers

The all-cause premature deaths attributed to BC increased from 733,910 cases (95% CI: 676,790-800,250) in 2000 to 903,030 cases (832,830-984,530) in 2005, decreased to 857,510 cases (790,500-935,370) in 2015, and finally reached the highest level at 937,980 cases (864,510-1,023,400) in 2020 (Figure 9). All-cause premature deaths attributed to BC of China in this work were estimated within the wide range of 50,100-1,436,960 cases by previous studies with different BC exposure levels and β_{BC} used (Cui et al., 2022; Qin et al., 2019; Saikawa et al., 2009; Wang et al., 2021). More premature deaths in eastern China (Supplementary Figure S8) were attributed mainly to the relatively high population density and premature death rate attributed to BC exposure from developed industrial and commercial activities (Supplementary Figure S9). The highest multiyear average of premature mortality was 1482 cases/1000 km^2 (the all-cause premature deaths attributed to BC per area of 1000 km^2) in Shanghai, followed by 793, 761, 520, 450, and 442 cases/1000 km^2 in Beijing, Tianjin, Jiangsu, Henan, and Shandong, respectively (Table 3). These values were much higher than the national average of 86 cases/1000 km^2.

Also shown in Figure 9 are the contributions of major factors to the national changing mortality during 2000-2020 (provincial-level results are presented in Table S13). The changing emission levels played an important role in premature mortality. Along with swift growth in the economy and energy consumption from 2000 to 2010, increasing BC emissions enhanced health risks in China and most provinces. The largest increase in national annual mortality was demonstrated during 2000-2005 (78,590 cases, 95% CI: 72,520-85,600). However, BC emission reductions in the main coal-producing provinces, i.e., Shanxi, Henan, and Sichuan, reduced regional health risks during 2005-2010, with declines in annual mortality of 14,320, 13,580, and 8,410 cases, respectively. Benefiting from improved air pollution controls from 2010 to 2020, declining health risks associated with BC emission reduction were demonstrated in China and most provinces. The largest decline in national annual mortality associated with BC emission reduction was demonstrated during 2010-2015 (133,360 cases, 123,150-145,180). BC emission rebound in Shanxi and Henan elevated regional health risks during 2015-2020, with increases in annual mortality of 7,170 and 6,190 cases, respectively.

Varying meteorological conditions also affected the health burden. With the exception of 2005-2010, meteorological conditions were estimated to increase BC exposure and the associated mortality for most of the research period, particularly in eastern China (Supplementary Figure S10). Among vulnerability factors, population aging contributed most to the increased BC-related health burden, elevating the annual national mortality by 99,800-142,310 cases for the various five-year intervals. Population growth contributed modestly to the increased health burden in most provinces, with annual national total changes of 10,940-21,230 cases. Exceptions included Sichuan and Hubei, where reduced populations resulted in declining mature mortality. Improved healthcare partly offset the adverse effect, with the annual avoided deaths increasing from 70,100 cases during 2000-2005 to 120,440 cases during 2010-2015. This positive effect shrank to 56,690 cases during 2015-2020. With increased population aging and reduced potential of medical care improvement, greater BC emission abatement will be needed to further prevent the health damage.

3.4 Uncertainty analysis

The uncertainties in our results are mainly attributed to separating the contribution of BC to AAOD, simulating BC AAOD based on WRF-CMAQ and the empirical light absorption model, lacking diurnal information of observed BC AAOD, and estimating the premature mortality attributable to BC. Due to the limited number of studies reporting spatiotemporal variability in BrC and dust light absorption in China, we separated BC AAOD based on the MERRA-2 dataset, which may underestimate BrC light absorption at 483 nm (Buchard et al., 2017). Herein, the multiyear average BrC share in AAOD was estimated at 16% (MERRA-2) in eastern China (Supplementary Figure S11), lower than that based on observations (18%–44%, Chen et al., 2019d; Li et al., 2019; Zhu et al., 2021). Notably, the multiyear average of posterior BC emissions using AAOD at a longer wavelength (865 nm) with little BrC effect was estimated to be 11% lower than that using 483 nm (Test 1 in Supplementary Text S3 and Figure 10). The posterior BC emissions based on the dust light absorption fraction to AAOD from Copernicus Atmosphere Monitoring Service (CAMS), which was only half that of MERRA-2 (Figure S3), were estimated to be very close to those of Test 1 (Test 2 in Text S3 and Figure 10). In addition, we adopted an empirical model based on observations from one city to simulate MAE. Even with improved performance compared to the average level of multiple CTMs at the global scale (Glıß et al., 2021), our model underestimated MAE and presented smaller regional heterogeneity than existing observations, likely due to the limited spatial extrapolation ability. When MAE was modified according to available observations across the country, the multiyear average of posterior BC emissions was estimated to be 10% lower than that without MAE modification (Test 3 in Text S3 and Figure 10). Besides, the removal processes in CMAQ also affect the BC lifetime simulation and thereby its atmospheric column concentration and emission inversion. The simulated lifetime of 4.7 days in the base case is within the range of 3.8~11.4 days reported by previous studies (Figure S4, Bond et al., 2013; Vignati et al., 2010). By adjusting the simulated BC lifetime to the multi-model average level (5.5 days, Glıß et al., 2021), the posterior emissions were estimated 4% smaller compared to those of the base case (Text S3 and Figure 10). Although modest uncertainties were revealed by the above sensitivity tests, they did not change the main findings of this study, with similar interannual variabilities between the base and sensitivity test cases (Figure 10). These uncertainties should be reduced with improved spatiotemporal coverage of BC, BrC and dust light-absorption observations. Another limitation of the inversion system came from the missing of diurnal information of observed AAOD. Since OMI could only provide AAOD at 13:30, we could not capture the diurnal distribution of BC emissions. Recently, the Geostationary Environment Monitoring Spectrometer (GEMS; Kim et al., 2020) was launched in 2020 and provided hourly daytime observations of aerosols. This can potentially be helpful for improving the temporal accuracy of BC emission inversion in the future.

Furthermore, the health impact estimation could be biased by rare domestic β_{BC} values in China. Previous studies commonly adopted the same functions as $PM_{2.5}$ (Saikawa et al., 2009) or β_{BC} values obtained from American or European studies (Wang et al., 2021), resulting in large uncertainty. Herein, we relied on a unique cohort study in China and calculated the all-cause premature deaths attributed to BC at 733,910-937,980/yr. The β_{BC} values obtained from national-scale studies in the US and Europe indicate a 10-fold difference (220,980-2,386,060/yr, Supplementary Table S14), similar to the estimation conducted in the US (Li et al., 2016b). More domestic epidemiological studies focusing on BC emissions are expected to further reduce the uncertainty.

4. Concluding remarks

Compared to previous studies with nonconsecutive or incomparable estimates, this study provides a panoramic view of the spatiotemporal patterns of AAOD, BC emissions, and the associated mortality in China for the past two decades. We found that the "bottom-up" approach likely underestimated BC emissions, particularly in less developed western and remote areas. Our findings also reveal the influence of human activities on the evolution of BC emissions and the remarkable emission abatement resulting from the implementation of national pollution controls, particularly in developed regions. Pollution controls were estimated to reduce the annual BC emissions by 26% during 2010-2020, reversing the 8% growth during 2000-2010. However, the benefits were smaller than those previously estimated employing the "bottom-up" approach, which likely overestimated progress in pollution controls for certain sources, like the transportation sector and residential solid fuel burning. The long-term BC emission trends in this study address both health and climate risks combined with the effects of other short-lived aerosol species.

The energy transition path to achieve China's goal of peak emissions and carbon neutrality provides an opportunity to further reduce BC emissions. Compared to developed regions, the energy transition and emission abatement is more challenging in coal-producing and less-urbanized regions, thus region-specific emission controls should be formulated. For the main coal-producing provinces, BC emissions have declined much slower than those in economically developed provinces or even rebounded along with increased industrial production capacity and energy demand in recent years. As China's traditional energy base, these provinces need to accelerate energy infrastructure adjustments and reduce their dependence on coal, through, for example, the development of photovoltaic and wind power. In addition, aggressively promoting advanced manufacturing technology is recommended. For example, expanding the coal-chemical industry chain could shift the role of coal consumption from traditional fuel to raw material, thus achieving its clean utilization (e.g., coal liquefaction and gasification technique). For less-urbanized regions, solid fuel, including coal, firewood, and crop residues, remain major energy sources, and actual BC emissions in rural areas could be greatly underestimated compared to those in urban areas. Expansion of natural gas and electricity use for cooking and heating could effectively limit BC emissions in these regions. These efforts can be supported through better infrastructure development and subsidy policy design in the future.

Data availability

The gap-filled AAOD and posterior BC emissions will be available at http://www.airqualitynju.com/En/Data/List/Datadownload once the paper is published.

Author contributions

WZhao developed the methodology, conducted the research, performed the analyses and wrote the draft. YZhao developed the strategy, designed the research and revised the manuscript. DChen and MMa provided the support of air quality modeling. HChe, YZhen, JXin, ZLi, KLi and YHang provided the support of AAOD data.

Competing interests

The authors declare that they have no conflict of interest.

Acknowledgements

This work was sponsored by the Natural Science Foundation of China (42177080) and the Key Research and Development Programme of Jiangsu Province (BE2022838). We thank Qiang Zhang from Tsinghua University for the emission data (MEIC) and Cheng Huang from Shanghai Academy of Environmental Sciences (SAES) for BC observation data. We also appreciate Jiandong Wang from Nanjing University of Information Science Information Science and Technology for advices on BC lifetime analysis.

REFERENCES

Ahn, C., Torres, O., and Bhartia, P. K.: Comparison of Ozone Monitoring Instrument UV Aerosol Products with Aqua/Moderate Resolution Imaging Spectroradiometer and Multiangle Imaging Spectroradiometer observations in 2006, J. Geophys. Res.-Atmos., 113, https://doi.org/10.1029/2007jd008832, 2008.

Bond, T. C., Doherty, S. J., Fahey, D. W., Forster, P. M., Berntsen, T., DeAngelo, B. J., Flanner, M. G., Ghan, S., Karcher, B., Koch, D., Kinne, S., Kondo, Y., Quinn, P. K., Sarofim, M. C., Schultz, M. G., Schulz, M., Venkataraman, C., Zhang, H., Zhang, S., Bellouin, N., Guttikunda, S. K., Hopke, P. K., Jacobson, M. Z., Kaiser, J. W., Klimont, Z., Lohmann, U., Schwarz, J. P., Shindell, D., Storelvmo, T., Warren, S. G., and Zender, C. S.: Bounding the role of black carbon in the climate system: A scientific assessment, J. Geophys. Res.-Atmos., 118, 5380-5552, https://doi.org/10.1002/jgrd.50171, 2013.

Buchard, V., Randles, C. A., da Silva, A. M., Darmenov, A., Colarco, P. R., Govindaraju, R., Ferrare, R., Hair, J., Beyersdorf, A. J., Ziemba, L. D., and Yu, H.: The MERRA-2 Aerosol Reanalysis, 1980 Onward. Part II: Evaluation and Case Studies, J. Clim., 30, 6851-6872, https://doi.org/10.1175/jcli-d-16-0613.1, 2017.

Che, H., Zhang, X. Y., Xia, X., Goloub, P., Holben, B., Zhao, H., Wang, Y., Zhang, X. C., Wang, H., Blarel, L., Damiri, B., Zhang, R., Deng, X., Ma, Y., Wang, T., Geng, F., Qi, B., Zhu, J., Yu, J., Chen, Q., and Shi, G.: Ground-based aerosol climatology of China: aerosol optical depths from the China Aerosol Remote Sensing Network (CARSNET) 2002-2013, Atmos. Chem. Phys., 15, 7619-7652, https://doi.org/10.5194/acp-15-7619-2015, 2015.

Chen, C., Dubovik, O., Henze, D. K., Chin, M., Lapyonok, T., Schuster, G. L., Ducos, F., Fuertes, D., Litvinov, P., Li, L., Lopatin, A., Hu, Q. Y., and Torres, B.: Constraining global aerosol emissions using POLDER/PARASOL satellite remote sensing observations, Atmos. Chem. Phys., 19, 14585-14606, https://doi.org/10.5194/acp-19-14585-2019, 2019a.

Chen, D., Zhao, Y., Lyu, R. T., Wu, R. R., Dai, L., Zhao, Y., Chen, F., Zhang, J., Yu, H., and Guan, M.: Seasonal and spatial variations of optical properties of light absorbing carbon and its influencing factors in a typical polluted city in Yangtze River Delta, China, Atmos. Environ., 199, 45-54, https://doi.org/10.1016/j.atmosenv.2018.11.022, 2019b.

Chen, L., Gao, Y., Zhang, M. G., Fu, J. S., Zhu, J., Liao, H., Li, J. L., Huang, K., Ge, B. Z., Wang, X. M., Lam, Y. F., Lin, C. Y., Itahashi, S., Nagashima, T., Kajino, M., Yamaji, K., Wang, Z. F., and Kurokawa, J.: MICS-Asia III: multi-model comparison and evaluation of aerosol over East Asia, Atmos. Chem. Phys., 19, 11911-11937, https://doi.org/10.5194/acp-19-11911-2019, 2019c.

Chen, S., Russell, L. M., Cappa, C. D., Zhang, X., Kleeman, M. J., Kumar, A., Liu, D., and Ramanathan, V.: Comparing black and brown carbon absorption from AERONET and surface measurements at wintertime Fresno, Atmos. Environ., 199, 164-176, https://doi.org/https://doi.org/10.1016/j.atmosenv.2018.11.032, 2019d.

Chen, Y., Chen, R., Chen, Y., Dong, X., Zhu, J., Liu, C., van Donkelaar, A., Martin, R. V., Li, H., Kan, H., Jiang, Q., and Fu, C.: The prospective effects of long-term exposure to ambient PM2.5 and constituents on mortality in rural East China, Chemosphere, 280, 130740, https://doi.org/10.1016/j.chemosphere.2021.130740, 2021.

Cohen, A. J., Brauer, M., Burnett, R., Anderson, H. R., Frostad, J., Estep, K., Balakrishnan, K., Brunekreef, B., Dandona, L., Dandona, R., Feigin, V., Freedman, G., Hubbell, B., Jobling, A., Kan, H., Knibbs, L., Liu, Y., Martin, R., Morawska, L., Pope, C. A., Shin, H., Straif, K., Shaddick, G., Thomas, M., van Dingenen, R., van Donkelaar, A., Vos, T., Murray, C. J. L., and Forouzanfar, M. H.: Estimates and 25-year trends of the global burden of disease attributable to ambient air pollution: an analysis of data from the Global Burden of Diseases Study 2015, The Lancet, 389, 1907-1918, https://doi.org/10.1016/s0140-6736(17)30505-6, 2017.

Cohen, J. B. and Wang, C.: Estimating global black carbon emissions using a top-down Kalman Filter approach, J. Geophys. Res.-Atmos., 119, 307-323, https://doi.org/10.1002/2013jd019912, 2014.

Cui, C., Liu, Y., Chen, L., Liang, S., Shan, M., Zhao, J., Liu, Y., Yu, S., Sun, Y., Mao, J., Zhang, H., Gao, S., and Ma, Z.: Assessing public health and economic loss associated with black carbon exposure using monitoring and MERRA-2 data, Environ. Pollut., 313, 120190, https://doi.org/10.1016/j.envpol.2022.120190, 2022.

Cui, H., Mao, P., Zhao, Y., Nielsen, C. P., and Zhang, J.: Patterns in atmospheric carbonaceous aerosols in China: emission estimates and observed concentrations, Atmos. Chem. Phys., 15, 8657-8678, https://doi.org/10.5194/acp-15-8657-2015, 2015.

Deborah, S. Z. and Pepijn, V.: OMI/Aura Multi-wavelength Aerosol Optical Depth and Single Scattering Albedo L3 1 day Best Pixel in 0.25 degree x 0.25 degree V3. NASA Goddard Space Flight Center, Goddard Earth Sciences Data and Information Services Center (GES DISC). Accessed: [10 March 2022], 10.5067/Aura/OMI/DATA3004, 2012.

European Commission, Joint Research Center (EC-JRC)/Netherlands Environmental Assessment Agency (PBL): Emissions Database for Global Atmospheric Research (EDGAR), release EDGAR v6.1_AP (1970 - 2018) of May 2022 [dataset], Accessed: [10 May 2023]. https://edgar.jrc.ec.europa.eu/dataset_ap61, 2022.

Evangeliou, N., Thompson, R. L., Eckhardt, S., and Stohl, A.: Top-down estimates of black carbon emissions at high latitudes using an atmospheric transport model and a Bayesian inversion framework, Atmos. Chem. Phys., 18, 15307-15327, https://doi.org/10.5194/acp-18-15307-2018, 2018.

Fu, T. M., Cao, J. J., Zhang, X. Y., Lee, S. C., Zhang, Q., Han, Y. M., Qu, W. J., Han, Z., Zhang, R., Wang, Y. X., Chen, D., and Henze, D. K.: Carbonaceous aerosols in China: top-down constraints on primary sources and estimation of secondary contribution, Atmos. Chem. Phys., 12, 2725-2746, https://doi.org/10.5194/acp-12-2725-2012, 2012.

Geng, G., Zheng, Y., Zhang, Q., Xue, T., Zhao, H., Tong, D., Zheng, B., Li, M., Liu, F., Hong, C., He, K., and Davis, S. J.: Drivers of PM2.5 air pollution deaths in China 2002–2017, Nat. Geosci., 14, 645–650, https://doi.org/10.1038/s41561-021-00792-3, 2021.

Glіß, J., Mortier, A., Schulz, M., Andrews, E., Balkanski, Y., Bauer, S. E., Benedictow, A. M. K., Bian, H., Checa-Garcia, R., Chin, M., Ginoux, P., Griesfeller, J. J., Heckel, A., Kipling, Z., Kirkevåg, A., Kokkola, H., Laj, P., Le Sager, P., Lund, M. T., Lund Myhre, C., Matsui, H., Myhre, G., Neubauer, D., van Noije, T., North, P., Olivié, D. J. L., Rémy, S., Sogacheva, L., Takemura, T., Tsigaridis, K., and Tsyro, S. G.: AeroCom phase III multi-model evaluation of the aerosol life cycle and optical properties using ground- and space-based remote sensing as well as surface in situ observations, Atmos. Chem. Phys., 21, 87-128, https://doi.org/10.5194/acp-21-87-2021, 2021.

Gu, Y. F., Zhang, W. S., Yang, Y. J., Wang, C., Streets, D. G., and Yim, S. H. L.: Assessing outdoor air quality and public health impact attributable to residential black carbon emissions in rural China, Resour Conserv Recy, 159, 104812, https://doi.org/10.1016/j.resconrec.2020.104812, 2020.

Guan, D., Liu, Z., Geng, Y., Lindner, S., and Hubacek, K.: The gigatonne gap in China’s carbon dioxide inventories, Nat. Clim. Change, 2, 672-675, https://doi.org/10.1038/nclimate1560, 2012.

Guerrette, J. J. and Henze, D. K.: Four-dimensional variational inversion of black carbon emissions during ARCTAS-CARB with WRFDA-Chem, Atmos. Chem. Phys., 17, 7605-7633, https://doi.org/10.5194/acp-17-7605-2017, 2017.

Han, Y. and Wang, Y.: Study on development, trend and countermeasures of coal industry in Shanxi province, China Economist, 318, 22-25 (in Chinese), 2015.

Harmsen, M. J. H. M., van Dorst, P., van Vuuren, D. P., van den Berg, M., Van Dingenen, R., and Klimont, Z.: Co-benefits of black carbon mitigation for climate and air quality, Clim. Change, 163, 1519-1538, https://doi.org/10.1007/s10584-020-02800-8, 2020.

Hu, Z. Y., Zhao, C., Huang, J. P., Leung, L. R., Qian, Y., Yu, H. B., Huang, L., and Kalashnikova, O. V.: Trans-Pacific transport and evolution of aerosols: evaluation of quasi-global WRF-Chem simulation with multiple observations, Geosci. Model Dev., 9, 1725-1746, https://doi.org/10.5194/gmd-9-1725-2016, 2016.

Huang, L., Zhu, Y., Zhai, H., Xue, S., Zhu, T., Shao, Y., Liu, Z., Emery, C., Yarwood, G., Wang, Y., Fu, J., Zhang, K., and Li, L.: Recommendations on benchmarks for numerical air quality model applications in China – Part 1: PM2.5 and chemical species, Atmos. Chem. Phys., 21, 2725-2743, https://doi.org/10.5194/acp-21-2725-2021, 2021.

Kim, J., Jeong, U., Ahn, M.-H., Kim, J. H., Park, R. J., Lee, H., Song, C. H., Choi, Y.-S., Lee, K.-H., Yoo, J.-M., Jeong, M.-J., Park, S. K., Lee, K.-M., Song, C.-K., Kim, S.-W., Kim, Y. J., Kim, S.-W., Kim, M., Go, S., Liu, X., Chance, K., Chan Miller, C., Al-Saadi, J., Veihelmann, B., Bhartia, P. K., Torres, O., Abad, G. G., Haffner, D. P., Ko, D. H., Lee, S. H., Woo, J.-H., Chong, H., Park, S. S., Nicks, D., Choi, W. J., Moon, K.-J., Cho, A., Yoon, J., Kim, S.-k., Hong, H., Lee, K., Lee, H., Lee, S., Choi, M., Veefkind, P., Levelt, P. F., Edwards, D. P., Kang, M., Eo, M., Bak, J., Baek, K., Kwon, H.-A., Yang, J., Park, J., Han, K. M., Kim, B.-R., Shin, H.-W., Choi, H., Lee, E., Chong, J., Cha, Y., Koo, J.-H., Irie, H., Hayashida, S., Kasai, Y., Kanaya, Y., Liu, C., Lin, J., Crawford, J. H., Carmichael, G. R., Newchurch, M. J., Lefer, B. L., Herman, J. R., Swap, R. J., Lau, A. K. H., Kurosu, T. P., Jaross, G., Ahlers, B., Dobber, M., McElroy, C. T., and Choi, Y.: New Era of Air Quality Monitoring from Space: Geostationary Environment Monitoring Spectrometer (GEMS), Bull. Am. Meteorol. Soc., 101, E1-E22, https://doi.org/10.1175/bams-d-18-0013.1, 2020.

Klimont, Z., Cofala, J., Xing, J., Wei, W., Zhang, C., Wang, S., Kejun, J., Bhandari, P., Mathur, R., Purohit, P., Rafaj, P., Chambers, A., Amann, M., and Hao, J.: Projections of SO2, NOx and carbonaceous aerosols emissions in Asia, Tellus B: Chem. Phys. Meteorol., 61B, 602-617, https://doi.org/10.1111/j.1600-0889.2009.00428.x, 2009.

Kurokawa, J. and Ohara, T.: Long-term historical trends in air pollutant emissions in Asia: Regional Emission inventory in ASia (REAS) version 3, Atmos. Chem. Phys., 20, 12761-12793, https://doi.org/10.5194/acp-20-12761-2020, 2020.

Lei, Y., Zhang, Q., He, K. B., and Streets, D. G.: Primary anthropogenic aerosol emission trends for China, 1990–2005, Atmos. Chem. Phys., 11, 931-954, https://doi.org/10.5194/acp-11-931-2011, 2011.

Li, M., Liu, H., Geng, G. N., Hong, C. P., Liu, F., Song, Y., Tong, D., Zheng, B., Cui, H. Y., Man, H. Y., Zhang, Q., and He, K. B.: Anthropogenic emission inventories in China: a review, Natl. Sci. Rev., 4, 834-866, https://doi.org/10.1093/nsr/nwx150, 2017.

Li, S. S., Yu, C., Chen, L. F., Tao, J. H., Letu, H., Ge, W., Si, Y. D., and Liu, Y.: Inter-comparison of model-simulated and satellite-retrieved componential aerosol optical depths in China, Atmos. Environ., 141, 320-332, https://doi.org/10.1016/j.atmosenv.2016.06.075, 2016a.

Li, Y., Henze, D. K., Jack, D., Henderson, B. H., and Kinney, P. L.: Assessing public health burden associated with exposure to ambient black carbon in the United States, Sci. Total Environ., 539, 515-525, https://doi.org/10.1016/j.scitotenv.2015.08.129, 2016b.

Li, Z., Tan, H., Zheng, J., Liu, L., Qin, Y., Wang, N., Li, F., Li, Y., Cai, M., Ma, Y., and Chan, C. K.: Light absorption properties and potential sources of particulate brown carbon in the Pearl River Delta region of China, Atmos. Chem. Phys., 19, 11669-11685, https://doi.org/10.5194/acp-19-11669-2019, 2019.

Li, Z. Q., Xu, H., Li, K. T., Li, D. H., Xie, Y. S., Li, L., Zhang, Y., Gu, X. F., Zhao, W., Tian, Q. J., Deng, R. R., Su, X. L., Huang, B., Qiao, Y. L., Cui, W. Y., Hu, Y., Gong, C. L., Wang, Y. Q., Wang, X. F., Wang, J. P., Du, W. B., Pan, Z. Q., Li, Z. Z., and Bu, D.: Comprehensive Study of Optical, Physical, Chemical, and Radiative Properties of Total Columnar Atmospheric Aerosols over China: An Overview of Sun–Sky Radiometer Observation Network (SONET) Measurements, Bull. Am. Meteorol. Soc., 99, 739-755, https://doi.org/10.1175/BAMS-D-17-0133.1, 2018.

Liang, F. C., Xiao, Q. Y., Huang, K. Y., Yang, X. L., Liu, F. C., Li, J. X., Lu, X. F., Liu, Y., and Gu, D. F.: The 17-y spatiotemporal trend of PM2.5 and its mortality burden in China, Proc. Natl. Acad. Sci. U.S.A., 117, 25601-25608, https://doi.org/10.1073/pnas.1919641117, 2020.

Liu, B., Tan, X., Jin, Y., Yu, W., and Li, C.: Application of RR-XGBoost combined model in data calibration of micro air quality detector, Sci. Rep., 11, 15662, https://doi.org/10.1038/s41598-021-95027-1, 2021.

Liu, S., Geng, G., Xiao, Q., Zheng, Y., Liu, X., Cheng, J., and Zhang, Q.: Tracking Daily Concentrations of PM2.5 Chemical Composition in China since 2000, Environ. Sci. Technol., 56, 16517–16527, https://doi.org/10.1021/acs.est.2c06510, 2022.

Liu, Y., Wang, M., Qian, Y., and Ding, A.: A Strong Anthropogenic Black Carbon Forcing Constrained by Pollution Trends Over China, Geophys. Res. Lett., 49, e2022GL098965, https://doi.org/10.1029/2022gl098965, 2022.

Louis, C., Liu, Y., Tassel, P., Perret, P., Chaumond, A., and André, M.: PAH, BTEX, carbonyl compound, black-carbon, NO2 and ultrafine particle dynamometer bench emissions for Euro 4 and Euro 5 diesel and gasoline passenger cars, Atmos. Environ., 141, 80-95, https://doi.org/10.1016/j.atmosenv.2016.06.055, 2016.

Lu, Y., Wang, Q. G., Zhang, X. H., Qian, Y., and Qian, X.: China's black carbon emission from fossil fuel consumption in 2015, 2020, and 2030, Atmos. Environ., 212, 201-207, https://doi.org/10.1016/j.atmosenv.2019.04.032, 2019.

Lu, Z., Zhang, Q., and Streets, D. G.: Sulfur dioxide and primary carbonaceous aerosol emissions in China and India, 1996–2010, Atmos. Chem. Phys., 11, 9839-9864, https://doi.org/10.5194/acp-11-9839-2011, 2011.

Lyu, B., Hu, Y., Zhang, W., Du, Y., Luo, B., Sun, X., Sun, Z., Deng, Z., Wang, X., Liu, J., Wang, X., and Russell, A. G.: Fusion Method Combining Ground-Level Observations with Chemical Transport Model Predictions Using an Ensemble Deep Learning Framework: Application in China to Estimate Spatiotemporally-Resolved PM2.5 Exposure Fields in 2014-2017, Environ. Sci. Technol., 53, 7306-7315, https://doi.org/10.1021/acs.est.9b01117, 2019.

McDuffie, E. E., Smith, S. J., O'Rourke, P., Tibrewal, K., Venkataraman, C., Marais, E. A., Zheng, B., Crippa, M., Brauer, M., and Martin, R. V.: A global anthropogenic emission inventory of atmospheric pollutants from sector- and fuel-specific sources (1970–2017): an application of the Community Emissions Data System (CEDS), Earth Syst. Sci. Data, 12, 3413-3442, https://doi.org/10.5194/essd-12-3413-2020, 2020.

Middleton, N.: Variability and Trends in Dust Storm Frequency on Decadal Timescales: Climatic Drivers and Human Impacts, Geosciences, 9, https://doi.org/10.3390/geosciences9060261, 2019.

Pani, S. K., Wang, S.-H., Lin, N.-H., Chantara, S., Lee, C.-T., and Thepnuan, D.: Black carbon over an urban atmosphere in northern peninsular Southeast Asia: Characteristics, source apportionment, and associated health risks, Environ. Pollut., 259, https://doi.org/10.1016/j.envpol.2019.113871, 2020.

Qin, Y. and Xie, S. D.: Spatial and temporal variation of anthropogenic black carbon emissions in China for the period 1980–2009, Atmos. Chem. Phys., 12, 4825-4841, https://doi.org/10.5194/acp-12-4825-2012, 2012.

Qin, Y., Fang, Y. Y., Li, X. Y., Naik, V., Horowitz, L. W., Liu, J. F., Scovronick, N., and Mauzerall, D. L.: Source attribution of black carbon affecting regional air quality, premature mortality and glacial deposition in 2000, Atmos. Environ., 206, 144-155, https://doi.org/10.1016/j.atmosenv.2019.02.048, 2019.

Saikawa, E., Naik, V., Horowitz, L. W., Liu, J., and Mauzerall, D. L.: Present and potential future contributions of sulfate, black and organic carbon aerosols from China to global air quality, premature mortality and radiative forcing, Atmos. Environ., 43, 2814-2822, https://doi.org/10.1016/j.atmosenv.2009.02.017, 2009.

Samset, B. H., Fuglestvedt, J. S., and Lund, M. T.: Delayed emergence of a global temperature response after emission mitigation, Nat. Commun., 11, 3261, https://doi.org/10.1038/s41467-020-17001-1, 2020.

Schroeder, W., Prins, E., Giglio, L., Csiszar, I., Schmidt, C., Morisette, J., and Morton, D.: Validation of GOES and MODIS active fire detection products using ASTER and ETM+ data, Remote Sens. Environ., 112, 2711-2726, https://doi.org/10.1016/j.rse.2008.01.005, 2008.

Schutgens, N., Dubovik, O., Hasekamp, O., Torres, O., Jethva, H., Leonard, P. J. T., Litvinov, P., Redemann, J., Shinozuka, Y., de Leeuw, G., Kinne, S., Popp, T., Schulz, M., and Stier, P.: AEROCOM and AEROSAT AAOD and SSA study - Part 1: Evaluation and intercomparison of satellite measurements, Atmos. Chem. Phys., 21, 6895-6917, https://doi.org/10.5194/acp-21-6895-2021, 2021.

Shindell, D., Kuylenstierna, J. C. I., Vignati, E., van Dingenen, R., Amann, M., Klimont, Z., Anenberg, S. C., Muller, N., Janssens-Maenhout, G., Raes, F., Schwartz, J., Faluvegi, G., Pozzoli, L., Kupiainen, K., Höglund-Isaksson, L., Emberson, L., Streets, D., Ramanathan, V., Hicks, K., Oanh, N. T. K., Milly, G., Williams, M., Demkine, V., and Fowler, D.: Simultaneously Mitigating Near-Term Climate Change and Improving Human Health and Food Security, Science, 335, 183-189, https://doi.org/doi:10.1126/science.1210026, 2012.

Streets, D. G., Yarber, K. F., Woo, J. H., and Carmichael, G. R.: Biomass burning in Asia: Annual and seasonal estimates and atmospheric emissions, Global Biogeochem. Cycles, 17, 1-20, https://doi.org/10.1029/2003gb002040, 2003.

Tao, J., Zhang, L., Cao, J., and Zhang, R.: A review of current knowledge concerning PM2. 5 chemical composition, aerosol optical properties and their relationships across China, Atmos. Chem. Phys., 17, 9485-9518, https://doi.org/10.5194/acp-17-9485-2017, 2017.

The Central People's Government of the People's Republic of China. Shanxi Province eliminated more than 200 million tons of backward coal production capacity from 2008 to 2010. Accessed: [20 January 2023]. http://www.gov.cn/jrzg/2011-05/12/content_1862911.htm., 2011.

Tsinghua University: The Multi-resolution Emission Inventory for China (MEIC) [dataset], Accessed: [25 May 2022]. http://meicmodel.org.cn. 2023.

United States Environmental Protection Agency: CMAQ (Version 5.1) (Software), Available from: https://zenodo.org/records/1079909, Accessed: [23 March 2021], 2017.

Vignati, E., Karl, M., Krol, M., Wilson, J., Stier, P., and Cavalli, F.: Sources of uncertainties in modelling black carbon at the global scale, Atmos. Chem. Phys., 10, 2595-2611, https://doi.org/10.5194/acp-10-2595-2010, 2010.

Wang, P., Wang, H., Wang, Y. Q., Zhang, X. Y., Gong, S. L., Xue, M., Zhou, C. H., Liu, H. L., An, X. Q., Niu, T., and Cheng, Y. L.: Inverse modeling of black carbon emissions over China using ensemble data assimilation, Atmos. Chem. Phys., 16, 989-1002, https://doi.org/10.5194/acp-16-989-2016, 2016.

Wang, R.: Global Emission Inventory and Atmospheric Transport of Black Carbon: Evaluation of the Associated Exposure., Springer, Berlin Heidelberg, 2015.

Wang, R., Andrews, E., Balkanski, Y., Boucher, O., Myhre, G., Samset, B. H., Schulz, M., Schuster, G. L., Valari, M., and Tao, S.: Spatial Representativeness Error in the Ground-Level Observation Networks for Black Carbon Radiation Absorption, Geophys. Res. Lett., 45, 2106-2114, https://doi.org/10.1002/2017GL076817, 2018.

Wang, R., Tao, S., Balkanski, Y., Ciais, P., Boucher, O., Liu, J., Piao, S., Shen, H., Vuolo, M. R., Valari, M., Chen, H., Chen, Y., Cozic, A., Huang, Y., Li, B., Li, W., Shen, G., Wang, B., and Zhang, Y.: Exposure to ambient black carbon derived from a unique inventory and high-resolution model, Proc. Natl. Acad. Sci. U.S.A., 111, 2459-2463, https://doi.org/10.1073/pnas.1318763111, 2014.

Wang, R., Tao, S., Wang, W., Liu, J., Shen, H., Shen, G., Wang, B., Liu, X., Li, W., Huang, Y., Zhang, Y., Lu, Y., Chen, H., Chen, Y., Wang, C., Zhu, D., Wang, X., Li, B., Liu, W., and Ma, J.: Black carbon emissions in China from 1949 to 2050, Environ. Sci. Technol., 46, 7595-7603, https://doi.org/10.1021/es3003684, 2012.

Wang, X., Wang, Y. X., Hao, J. M., Kondo, Y., Irwin, M., Munger, J. W., and Zhao, Y. J.: Top-down estimate of China's black carbon emissions using surface observations: Sensitivity to observation representativeness and transport model error, J. Geophys. Res.-Atmos., 118, 5781-5795, https://doi.org/10.1002/jgrd.50397, 2013.

Wang, Y., Li, X., Shi, Z., Huang, L., Li, J., Zhang, H., Ying, Q., Wang, M., Ding, D., Zhang, X., and Hu, J.: Premature Mortality Associated with Exposure to Outdoor Black Carbon and Its Source Contributions in China, Resour. Conserv. Recycl., 170, 105620, https://doi.org/10.1016/j.resconrec.2021.105620, 2021.

Wang, Y., Zhao, Y., Liu, Y., Jiang, Y., Zheng, B., Xing, J., Liu, Y., Wang, S., and Nielsen, C. P.: Sustained emission reductions have restrained the ozone pollution over China, Nat. Geosci., 16, 967-974, https://doi.org/10.1038/s41561-023-01284-2, 2023.

WorldPop (www.worldpop.org - School of Geography and Environmental Science, University of Southampton; Department of Geography and Geosciences, University of Louisville; Departement de Geographie, Universite de Namur) and Center for International Earth Science Information Network (CIESIN), Columbia University. Accessed: [20 October 2022], https://dx.doi.org/10.5258/SOTON/WP00674, 2018.

Xiao, Q. Y., Chang, H. H., Geng, G. N., and Liu, Y.: An Ensemble Machine-Learning Model To Predict Historical PM2.5 Concentrations in China from Satellite Data, Environ. Sci. Technol., 52, 13260-13269, https://doi.org/10.1021/acs.est.8b02917, 2018.

Xin, J., Wang, Y., Pan, Y., Ji, D., Liu, Z., Wen, T., Wang, Y., Li, X., Sun, Y., Sun, J., Wang, P., Wang, G., Wang, X., Cong, Z., Song, T., Hu, B., Wang, L., Tang, G., Gao, W., Guo, Y., Miao, H., Tian, S., and Wang, L.: The Campaign on Atmospheric Aerosol Research Network of China: CARE-China, Bull. Am. Meteorol. Soc., 96, 1137-1155, https://doi.org/10.1175/BAMS-D-14-00039.1, 2015.

Xu, X., Yang, X., Zhu, B., Tang, Z., Wu, H., and Xie, L.: Characteristics of MERRA-2 black carbon variation in east China during 2000–2016, Atmos. Environ., 222, 117140, https://doi.org/https://doi.org/10.1016/j.atmosenv.2019.117140, 2020.

Xue, T., Zheng, Y., Li, X., Liu, J., Zhang, Q., and Zhu, T.: A component-specific exposure-mortality model for ambient PM2.5 in China: findings from nationwide epidemiology based on outputs from a chemical transport model, Faraday Discuss., 226, 551-568, https://doi.org/10.1039/d0fd00093k, 2021.

Yang, J., Zhao, T. L., Cheng, X. G., Ren, Z. H., Meng, L., He, Q., Tan, C. H., Zhu, Y., Zhu, C. Z., and Wu, Z. Y.: Temporal and spatial variations of sandstorm and the related meteorological influences over northern China from 2000 to 2019, Acta Sci. Circum., 41, 2966-2975 (in Chinese), https://doi.org/10.13671/j.hjkxxb.2021.0234, 2021.

Yang, Y. and Zhao, Y.: Quantification and evaluation of atmospheric pollutant emissions from open biomass burning with multiple methods: a case study for the Yangtze River Delta region, China, Atmos. Chem. Phys., 19, 327-348, https://doi.org/10.5194/acp-19-327-2019, 2019.

Zhang, L., Henze, D. K., Grell, G. A., Carmichael, G. R., Bousserez, N., Zhang, Q., Torres, O., Ahn, C., Lu, Z., Cao, J., and Mao, Y.: Constraining black carbon aerosol over Asia using OMI aerosol absorption optical depth and the adjoint of GEOS-Chem, Atmos. Chem. Phys., 15, 10281-10308, https://doi.org/10.5194/acp-15-10281-2015, 2015.

Zhang, L., Henze, D. K., Grell, G. A., Torres, O., Jethva, H., and Lamsal, L. N.: What factors control the trend of increasing AAOD over the United States in the last decade?, J. Geophys. Res.-Atmos., 122, 1797-1810, https://doi.org/10.1002/2016jd025472, 2017.

Zhang, Q., Zheng, Y., Tong, D., Shao, M., Wang, S., Zhang, Y., Xu, X., Wang, J., He, H., Liu, W., Ding, Y., Lei, Y., Li, J., Wang, Z., Zhang, X., Wang, Y., Cheng, J., Liu, Y., Shi, Q., Yan, L., Geng, G., Hong, C., Li, M., Liu, F., Zheng, B., Cao, J., Ding, A., Gao, J., Fu, Q., Huo, J., Liu, B., Liu, Z., Yang, F., He, K., and Hao, J.: Drivers of improved PM2.5 air quality in China from 2013 to 2017, Proc. Natl. Acad. Sci. U.S.A., 116, 24463-24469, https://doi.org/10.1073/pnas.1907956116, 2019.

Zhao, X. F., Zhao, Y., Chen, D., Li, C. Y., and Zhang, J.: Top-down estimate of black carbon emissions for city clusters using ground observations: a case study in southern Jiangsu, China, Atmos. Chem. Phys., 19, 2095-2113, https://doi.org/10.5194/acp-19-2095-2019, 2019.

Zheng, B., Geng, G., Ciais, P., Davis Steven, J., Martin Randall, V., Meng, J., Wu, N., Chevallier, F., Broquet, G., Boersma, F., van der, A. R., Lin, J., Guan, D., Lei, Y., He, K., and Zhang, Q.: Satellite-based estimates of decline and rebound in China's CO2 emissions during COVID-19 pandemic, Sci. Adv., 6, eabd4998, https://doi.org/10.1126/sciadv.abd4998, 2020.

Zhi, G., Zhang, Y., Sun, J., Cheng, M., Dang, H., Liu, S., Yang, J., Zhang, Y., Xue, Z., Li, S., and Meng, F.: Village energy survey reveals missing rural raw coal in northern China: Significance in science and policy, Environ. Pollut., 223, 705-712, https://doi.org/10.1016/j.envpol.2017.02.009, 2017.

Zhu, C. S., Qu, Y., Huang, H., Chen, J., Dai, W. T., Huang, R. J., and Cao, J. J.: Black Carbon and Secondary Brown Carbon, the Dominant Light Absorption and Direct

Radiative Forcing Contributors of the Atmospheric Aerosols Over the Tibetan Plateau, Geophys. Res. Lett., 48, 1-9, https://doi.org/10.1029/2021gl092524, 2021.

Zhu, X., Yun, X., Meng, W., Xu, H., Du, W., Shen, G., Cheng, H., Ma, J., and Tao, S.: Stacked Use and Transition Trends of Rural Household Energy in Mainland China, Environ. Sci. Technol., 53, 521-529, https://doi.org/10.1021/acs.est.8b04280, 2019.

Figure captions

Figure 1 The top-down inversion approach to estimate monthly BC emissions.

Figure 2 Comparison between XGBoost predicted and OMI observed AAOD for 2005-2020. Different colors of dots represent values for different years. The red dashed line indicates the 1:1 line. The blue dashed line indicates the regression line. The interval of bins of the marginal histograms is 0.02.

Figure 3 (a) Spatial distribution of multiyear average AAOD during 2000-2020 and (b-h) interannual variations of AAOD for China and six key regions in 2000-2020. The grey and white present Phase 1 (2000-2012) and Phase 2 (2013-2020), respectively. The red dots and dashed line represent time series of monthly AAOD (left vertical axis). The black solid lines represent the interannual variability after removing the seasonal change through time-series decomposition (right vertical axis). The straight red and blue lines present the linear trends of AAOD for different phases (right vertical axis). The annual variation rates (1/yr) during different phases with significance levels (*p < 0.05, **p < 0.01, ***p < 0.001) are presented.

Figure 4 Correlation between simulated and observed monthly surface BC concentrations in China. Simulations were conducted based on prior and posterior BC emissions, while observations were collected from publications.

Figure 5 Comparisons between posterior and various “bottom-up” BC emission estimates in China during 2000-2020. (a) Multiyear average spatial distribution of prior BC emissions (MEIC+GFED), (b) posterior BC emissions, and (c) their relative differences. (d) Long-term variability in the relative differences between posterior and various “bottom-up” BC emission estimates, with five-year intervals. Note: OBB emissions from GFED are added to each anthropogenic emission estimate as the total “bottom-up” estimate, except for PKU-Fuel, Lu et al. (2011) and Qin and Xie (2012) which include their own OBB emission estimate. (e) Long-term variability in normalized posterior and various “bottom-up” BC emission estimates (relative to 2000). The grey area indicates the period with declining national BC emissions. (f) Long-term variability in the relative differences between prior (MEIC+GFED) and posterior BC emissions by region and land use type.

Figure 6 The annual (a) prior BC emissions, (b) posterior BC emissions (three times of total emissions of January, April, July and October) and (c) their relative differences during 2000-2020 (with a five-year interval).

Figure 7 Changes in provincial BC emission intensity (annual BC emissions per km2) in posterior BC estimates. (a,b) Spatial distribution of the interannual change rate of BC emission intensity by province during 2000-2010 and 2010-2020. (c,d) Relationships between interannual BC emission intensity change rate and rural population fraction, proportion of coal production, and industrial GDP for each province. The x and y-axes present the rural population fraction of each province and provincial proportion of coal production to the national total for the middle year of the concerned period (i.e., 2005 for c and 2015 for d), respectively. Circle size represents provincial industrial GDP level. The colors in (c) and (d) are the same as those in (a) and (b). Statistics of population, coal production, and GDP were obtained from the National Bureau of Statistics (https://data.stats.gov.cn/; last accessed on 15 February 2023).

Figure 8 Relative changes of the prior and posterior BC, OC, $PM_{2.5}$ emissions (left vertical axis) and the posterior BC and $PM_{2.5}$ concentrations (right vertical axis) during 2000-2020 compared with those of 2000 (with a five-year interval). OC and $PM_{2.5}$ emissions are obtained from the Multi-resolution Emission Inventory for China (MEIC, http://www.meicmodel.org; last access: 25 May 2022). $PM_{2.5}$ concentrations are obtained from Tracking Air Pollution in China (TAP, http://tapdata.org.cn/; last access: 31 January 2023).

Figure 9 Total all-cause premature deaths attributed to BC exposure in China (grey bars) and drivers of changing premature mortality (colored bars) during 2000-2020 (with a 5-year interval). Error bars show the 95% CI of estimates in this study. The numbers of total all-cause premature deaths are at the bottom of the Figure. The contributions of major factors to the national changing mortality are above the colored bars.

Figure 10 (a) Long-term variability of the normalized prior and posterior BC emissions in China during 2000-2020 (compared with 2000, solid lines with left vertical axis, with a five-year interval), and relative difference between the posterior and prior emissions (dashed lines with right vertical axis) for the base case, Test 1, Test 2, Test 3 and Test 4. (b) Relative difference in the Eastern China and the rest of China for the base case (red lines and marks), Test 1 (green lines and marks), Test 2 (purple lines and marks), Test 3 (blue lines and marks) and Test 4 (yellow lines and marks).

Tables

Table 1 The multiyear average relative differences between the posterior and various "bottom-up" estimates of BC emissions by region (unitless). Note: OBB emissions from GFED are added to each anthropogenic emission estimates as the total "bottom-up" estimate, except for PKU-Fuel which includes its own OBB emission estimate.

Region	CEDS + GFED	PKU-Fuel	EDGAR + GFED	REAS + GFED	MEIC + GFED	Average
BTH	1.19	0.31	2.35	0.69	0.99	1.11
FWP	2.18	0.56	3.63	1.50	2.70	2.11
YRD	0.80	1.44	1.23	1.49	1.56	1.30
PRD	0.75	1.15	2.01	2.05	2.65	1.72
SCB	3.23	2.23	6.38	3.01	3.17	3.60
NE	4.90	4.66	6.37	5.36	6.81	5.62
Other	3.35	1.98	4.96	3.68	3.62	3.52
China	2.68	1.72	4.13	2.82	3.26	2.92

Table 2 The annual posterior BC emission intensity of different land-use types in 2000-2020 (with a five-year interval). The annual emission intensity was estimated as three times sum of BC emission intensity of January, April, July and October. "Urban" includes city and building categories, and "Rural" includes cropland and countryside categories (Unit: $Mg/km^2/yr$).

	2000	2005	2010	2015	2020	Average
City	2.26	2.19	2.32	1.98	1.68	2.09
Building	1.57	1.70	1.68	1.42	1.23	1.52
Countryside	1.59	1.74	1.77	1.66	1.43	1.64
Cropland	1.46	1.61	1.60	1.37	1.22	1.45
Forest	0.89	0.93	0.97	0.71	0.70	0.84
Grassland	0.35	0.39	0.35	0.27	0.27	0.33
Unused	0.11	0.13	0.12	0.11	0.09	0.11
Urban	1.98	1.99	2.07	1.75	1.50	1.86
Rural	1.47	1.62	1.62	1.39	1.24	1.47

Table 3 The annual all-cause premature mortality associated with BC exposure by province in mainland China during 2000-2020 with a five-year interval (Unit: cases/1000 km^2). Locations of provinces are shown in Figure S1a.

	2000	2005	2010	2015	2020	Average
Shanghai	1050	1258	1661	2038	1403	1482
Beijing	410	686	781	930	1156	793
Tianjin	442	601	760	907	1094	761
Jiangsu	341	481	575	669	535	520
Henan	386	484	421	404	555	450
Shandong	299	433	455	494	529	442
Anhui	218	320	338	341	322	308
Liaoning	346	282	271	234	226	272
Hebei	194	250	238	249	303	247
Chongqing	253	285	249	204	239	246
Hubei	173	250	245	192	210	214
Jilin	207	200	206	212	188	203
Zhejiang	140	180	210	234	224	198
Hunan	163	227	206	171	216	197
Guangdong	149	177	213	165	192	179
Shanxi	192	213	134	130	217	177
Sichuan	124	148	130	105	113	124
Guizhou	109	128	111	120	132	120
Jiangxi	90	127	129	108	136	118
Shannxi	97	120	95	80	116	101
Heilongjiang	87	88	104	113	109	100
Fujian	81	87	99	79	84	86
Guangxi	70	96	99	72	81	84
Hainan	46	59	64	43	59	54
Yunnan	42	51	49	50	59	50
Ningxia	34	49	33	34	49	40
Gansu	23	30	19	17	22	22
Inner Mongolia	6	8	6	5	7	7
Qinghai	2	3	2	2	2	2
Xinjiang	1	1	1	1	1	1
Tibet	0	0	0	0	0	0

Figures

Figure 1 The top-down inversion approach to estimate monthly BC emissions.

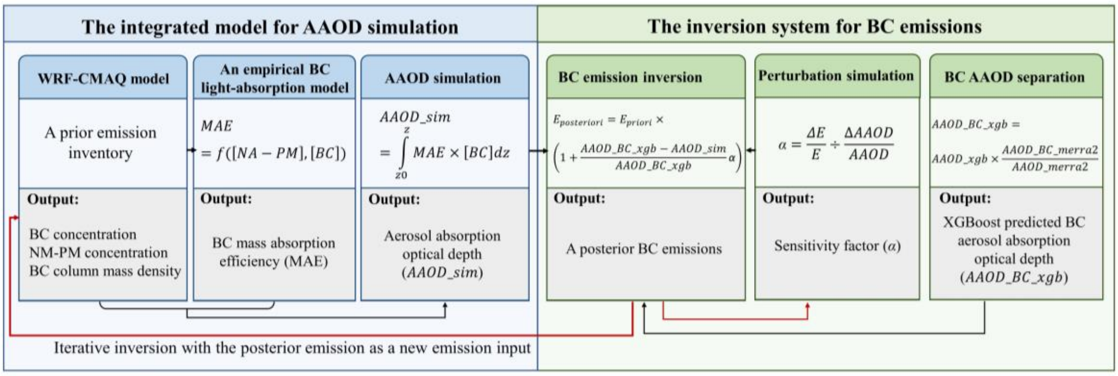

Figure 2 Comparison between XGBoost predicted and OMI observed AAOD for 2005-2020. Different colors of dots represent values for different years. The red dashed line indicates the 1:1 line. The blue dashed line indicates the regression line. The interval of bins of the marginal histograms is 0.02.

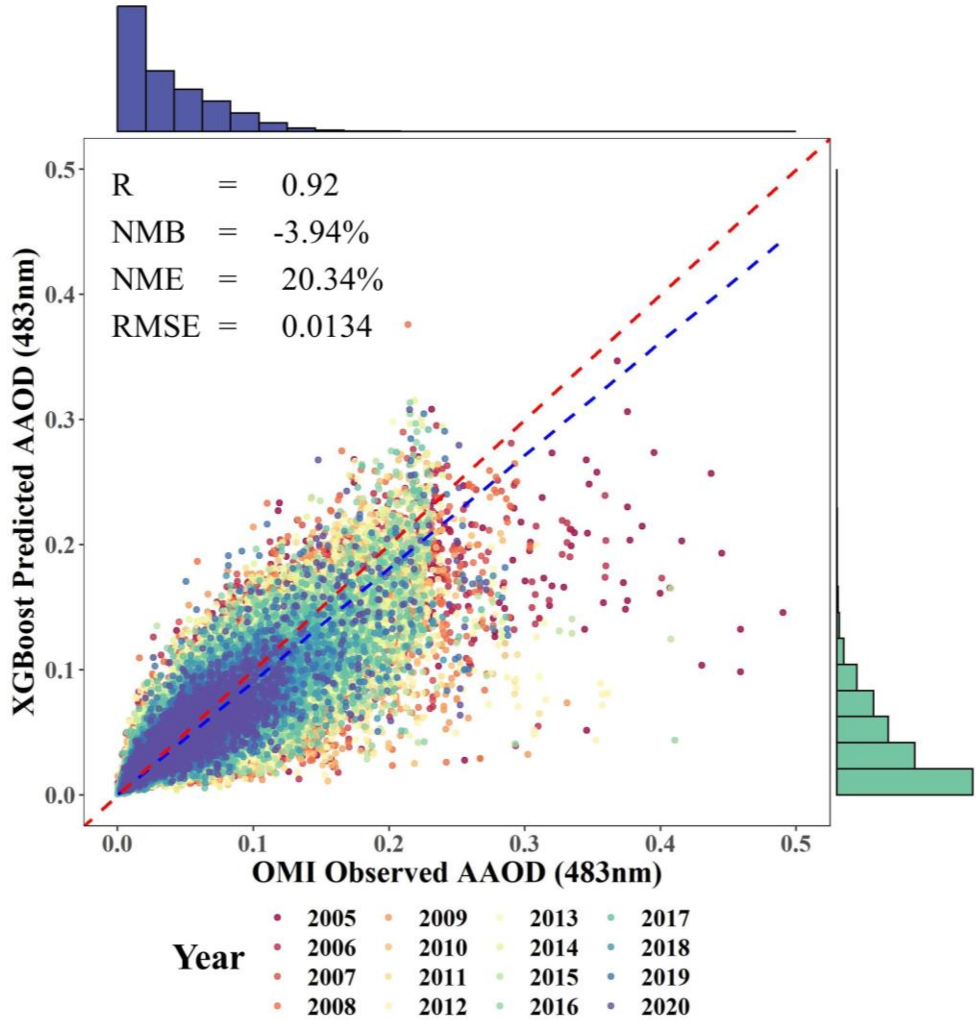

Figure 3 (a) Spatial distribution of multiyear average AAOD during 2000-2020 and (b-h) interannual variations of AAOD for China and six key regions in 2000-2020. The grey and white present Phase 1 (2000-2012) and Phase 2 (2013-2020), respectively. The red dots and dashed line represent time series of monthly AAOD (left vertical axis). The black solid lines represent the interannual variability after removing the seasonal change through time-series decomposition (right vertical axis). The straight red and blue lines present the linear trends of AAOD for different phases (right vertical axis). The annual variation rates (1/yr) during different phases with significance levels (*p < 0.05, **p < 0.01, ***p < 0.001) are presented.

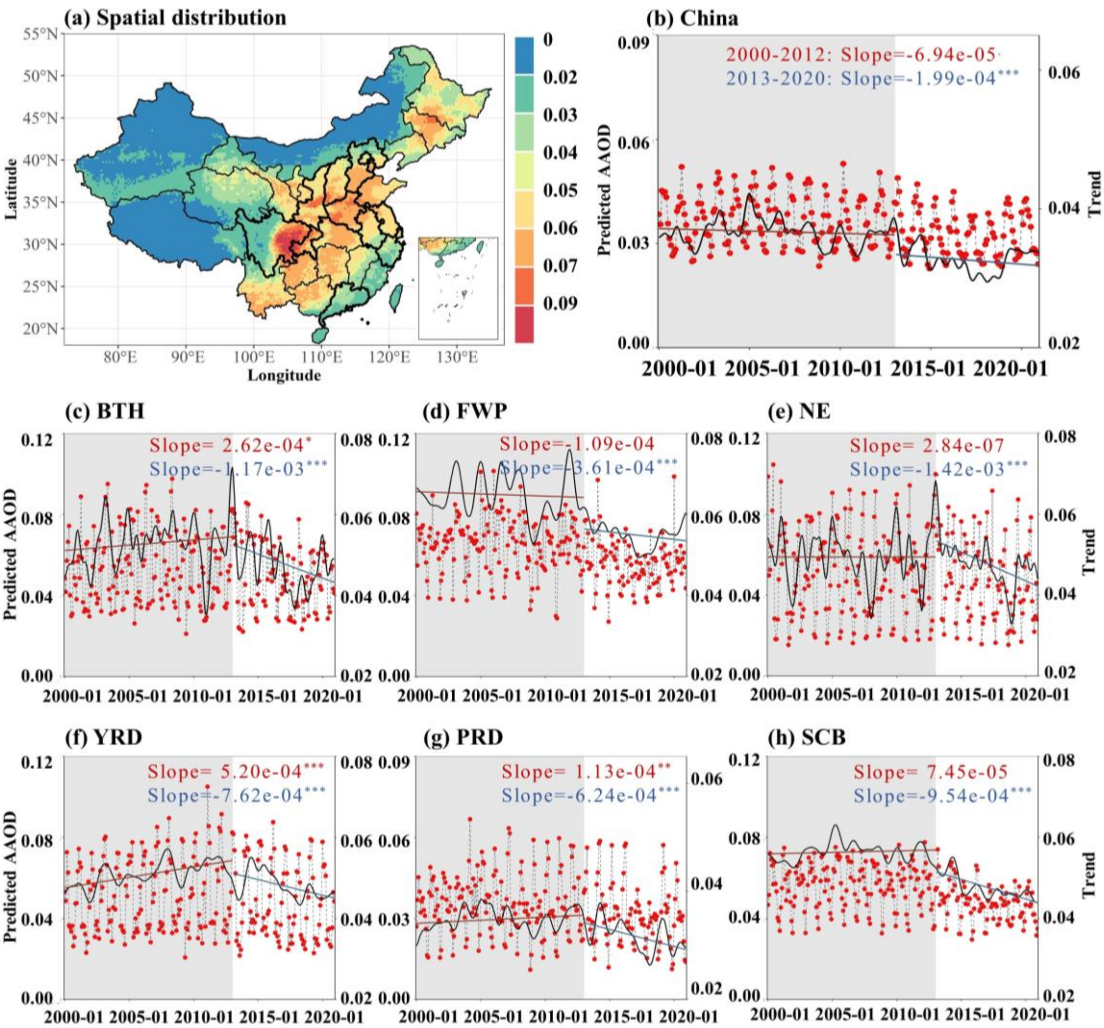

Figure 4 **Correlation between simulated and observed monthly surface BC concentrations in China. Simulations were conducted based on prior and posterior BC emissions, while observations were collected from publications.**

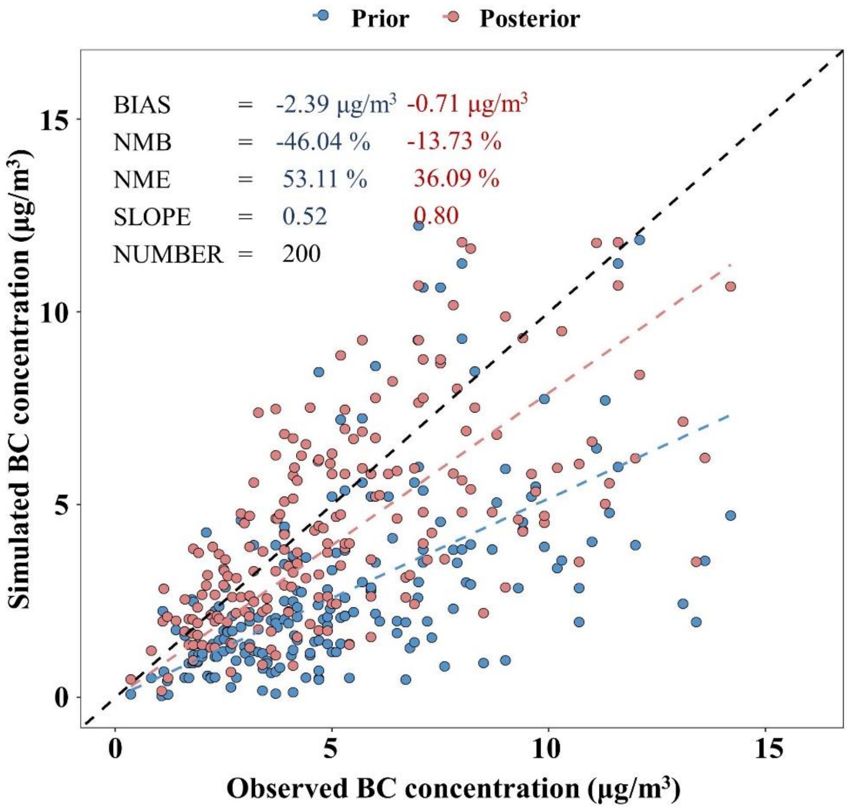

Figure 5 Comparisons between posterior and various "bottom-up" BC emission estimates in China during 2000-2020. (a) Multiyear average spatial distribution of prior BC emissions (MEIC+GFED), (b) posterior BC emissions, and (c) their relative differences. (d) Long-term variability in the relative differences between posterior and various "bottom-up" BC emission estimates, with five-year intervals. Note: OBB emissions from GFED are added to each anthropogenic emission estimate as the total "bottom-up" estimate, except for PKU-Fuel, Lu et al. (2011) and Qin and Xie (2012) which include their own OBB emission estimate. (e) Long-term variability in normalized posterior and various "bottom-up" BC emission estimates (relative to 2000). The grey area indicates the period with declining national BC emissions. (f) Long-term variability in the relative differences between prior (MEIC+GFED) and posterior BC emissions by region and land use type.

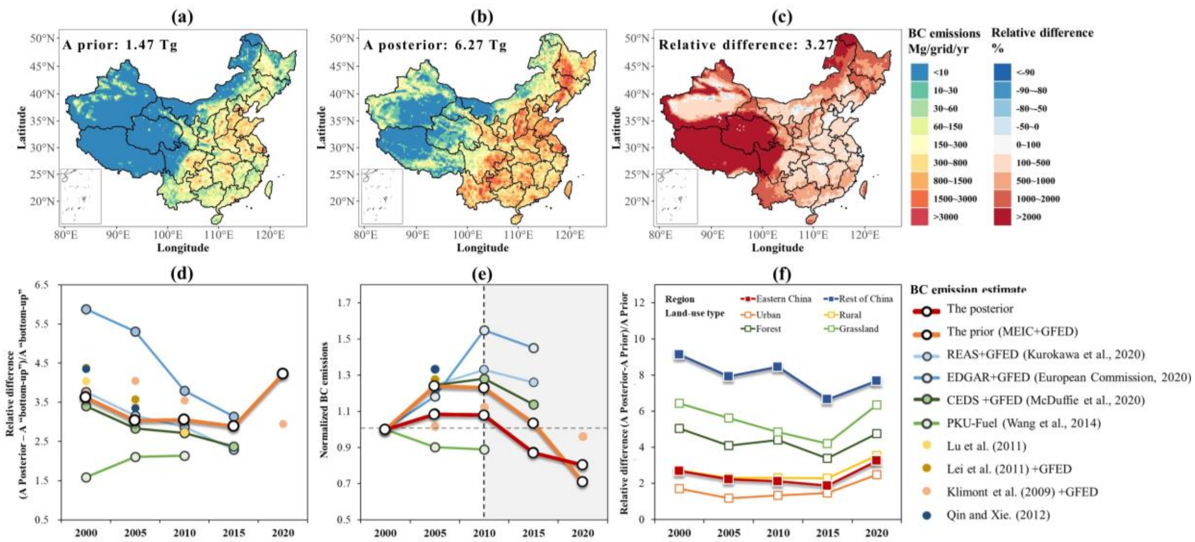

Figure 6 **The annual (a) prior BC emissions, (b) posterior BC emissions (three times of total emissions of January, April, July and October) and (c) their relative differences during 2000-2020 (with a five-year interval).**

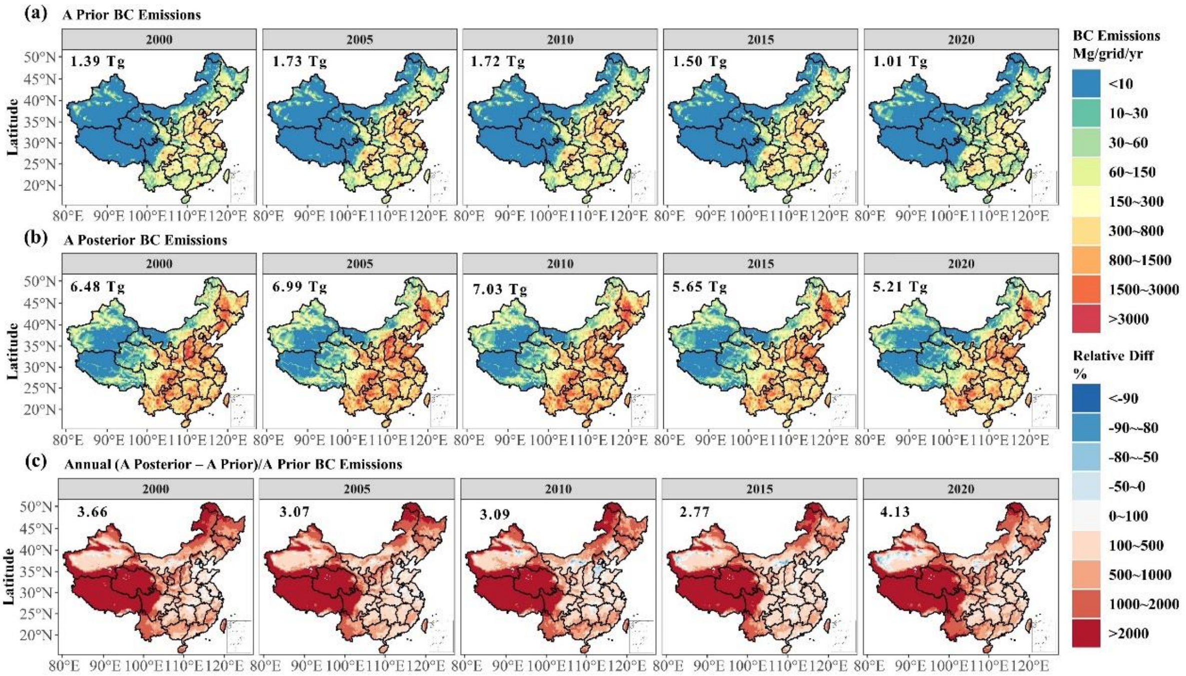

Figure 7 Changes in provincial BC emission intensity (annual BC emissions per km^2) in posterior BC estimates. (a,b) Spatial distribution of the interannual change rate of BC emission intensity by province during 2000-2010 and 2010-2020. (c,d) Relationships between interannual BC emission intensity change rate and rural population fraction, proportion of coal production, and industrial GDP for each province. The x and y-axes present the rural population fraction of each province and provincial proportion of coal production to the national total for the middle year of the concerned period (i.e., 2005 for c and 2015 for d), respectively. Circle size represents provincial industrial GDP level. The colors in (c) and (d) are the same as those in (a) and (b). Statistics of population, coal production, and GDP were obtained from the National Bureau of Statistics (https://data.stats.gov.cn/; last accessed on 15 February 2023).

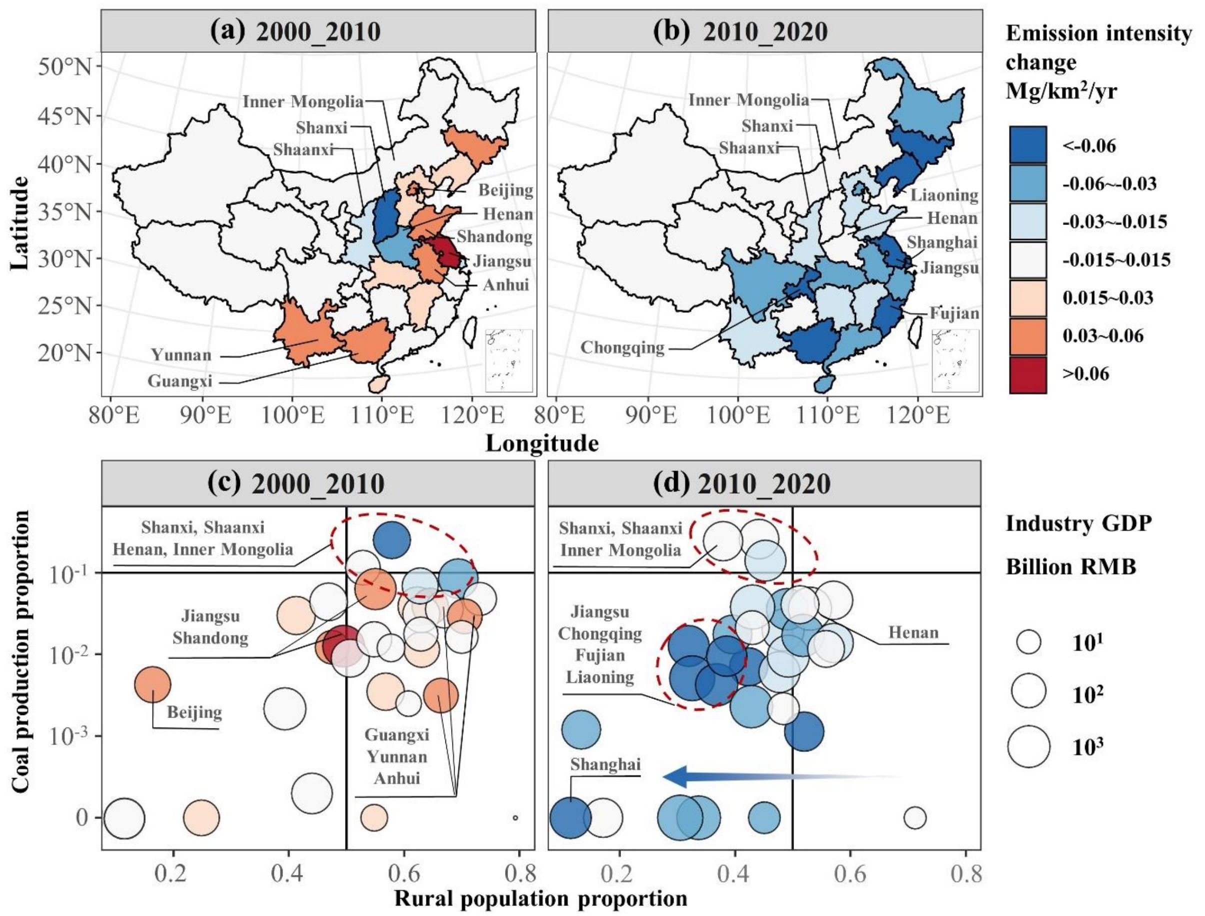

Figure 8 Relative changes of the prior and posterior BC, OC, $PM_{2.5}$ emissions (left vertical axis) and the posterior BC and $PM_{2.5}$ concentrations (right vertical axis) during 2000-2020 compared with those of 2000 (with a five-year interval). OC and $PM_{2.5}$ emissions are obtained from the Multi-resolution Emission Inventory for China (MEIC, http://www.meicmodel.org; last access: 25 May 2022). $PM_{2.5}$ concentrations are obtained from Tracking Air Pollution in China (TAP, http://tapdata.org.cn/; last access: 31 January 2023).

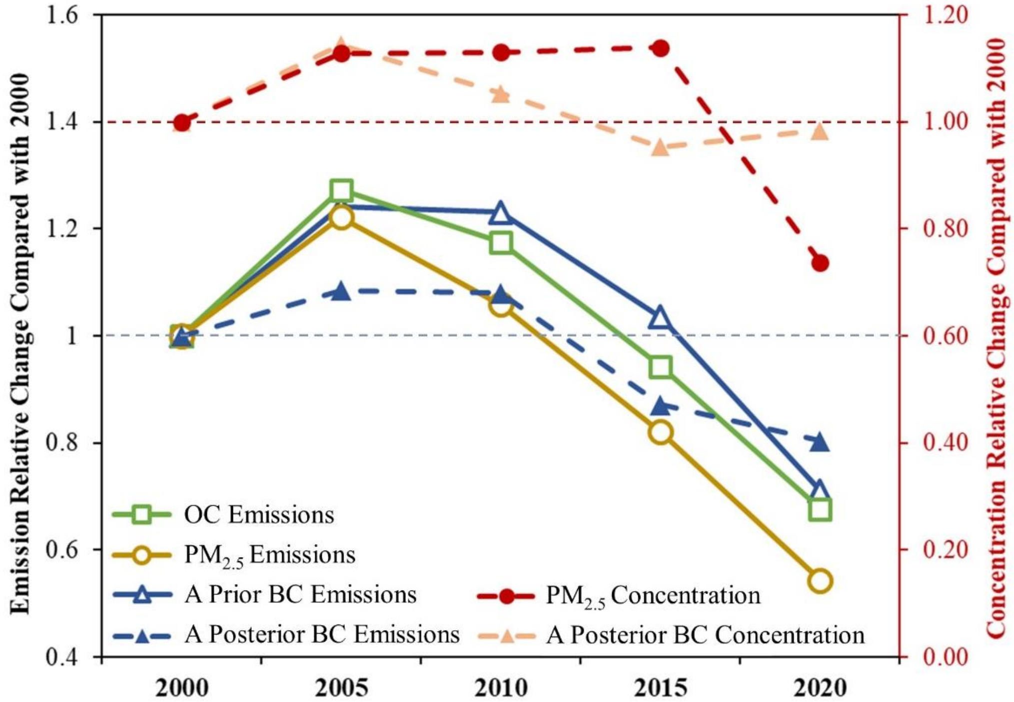

Figure 9 Total all-cause premature deaths attributed to BC exposure in China (grey bars) and drivers of changing premature mortality (colored bars) during 2000-2020 (with a 5-year interval). Error bars show the 95% CI of estimates in this study. The numbers of total all-cause premature deaths are at the bottom of the Figure. The contributions of major factors to the national changing mortality are above the colored bars.

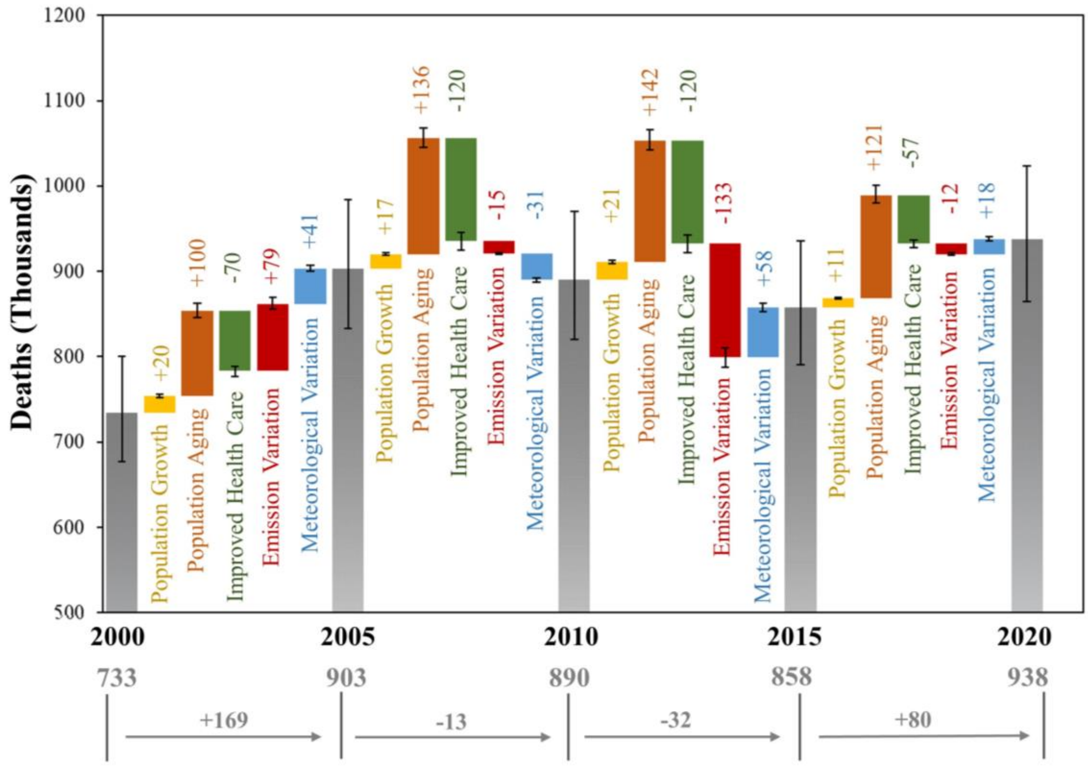

Figure 10 (a) Long-term variability of the normalized prior and posterior BC emissions in China during 2000-2020 (compared with 2000, solid lines with left vertical axis, with a five-year interval), and relative difference between the posterior and prior emissions (dashed lines with right vertical axis) for the base case, Test 1, Test 2, Test 3 and Test 4. (b) Relative difference in the Eastern China and the rest of China for the base case (red lines and marks), Test 1 (green lines and marks), Test 2 (purple lines and marks), Test 3 (blue lines and marks) and Test 4 (yellow lines and marks).